Laser shock peening

Journal of Physics: Conference Series **1787** (2021) 012024 doi:10.1088/1742-6596/1787/1/012024

Laser shock peening

N A Inogamov[1,2,3], V V Zhakhovsky[2,3], D K Ilnitsky[2] and V A Khokhlov[1]

[1] Landau Institute for Theoretical Physics of the Russian Academy of Sciences, Akademika Semenova 1a, Chernogolovka, Moscow Region 142432, Russia
[2] Dukhov Research Institute of Automatics (VNIIA), Sushchevskaya 22, Moscow 127055, Russia
[3] Joint Institute for High Temperatures of the Russian Academy of Sciences, Izhorskaya 13 Bldg 2, Moscow 125412, Russia

E-mail: nailinogamov@gmail.com

Abstract. Elastic-plastic transformations together with or separately of polymorphic phase transitions are important for the theory of shock waves. Here we discuss changing a classification consisting from elastic, split elastic-plastic, and pure plastic shocks. The split shocks means that there are two jumps: the elastic precursor and plastic shock, and that the elastic jump is independent relative to plastic one. In the split regime the precursor moves with elastic speed of sound overrunning the plastic jump and going further and further ahead relative to plastic jump as time proceeds and becoming weaker and weaker. We oppose the split shock to the one-wave (1W) two zones (elastic and plastic—2Z) shock (1W2Z shock). The 1W2Z wave propagates as whole (therefore one-wave), the plastic shock dynamically supports the elastic one, and the average distance between the jumps does not change in time. The powerful elastic shocks (their amplitudes are much higher than are usually suggested for elastic shocks) were found in experiments with femtosecond laser pulses and confirmed in large scale molecular dynamics (MD) simulations. The observation of the 1W2Z shocks is another important finding coming from MD. The report is devoted to lasers, shocks, and applications. In the second part of the report the generation and propagation of the shocks created for laser shock peening by lasers with ultrashort or nanosecond pulses are considered.

1. Introduction

Studies of shock waves cover a very wide range of physical problems from hydrodynamics where the shocks complicate many flows (see, e.g., [1]—implosive collapse) to kinetic processes defining internal structure of a shock front (see, e.g., [2, 3]). There are diversed scientific directions from collisionless shocks in rarefied hot plasma [4] to elastic-plastic and–or polymorphic transformations in solids [2, 5–15]. Shocks in a targets with a boundary are accompanied by rarefaction waves causing spallation in condensed media [10, 12, 13, 16, 17]. Powerful laser shocks are used to explore equations of thermodynamic states of matter [18]. Lasers are used for structuring [19–23] and generation of nanoparticles [20, 21, 24–26]. These stories are listed to show the base from which the report has been developed.

Elastic-plastic phenomena are important primarily for the mechanics of deformable solids. Theories of creep and plastic motions often are formal, purely mathematical in nature. At the same time, they are based on empirical measurements such as measurements of a bulk modulus B, a strength of materials or a yield stress Y.

Powerful and relatively new approaches for studies in this branch of sciences are connected with molecular dynamics. These approaches allow us to see what is going on interatomic level, how the coordinated motions of ensembles of atoms takes forms of nucleating and evolving dislocations. It is not possible to achieve such resolutions in experiments, even using ultrashort (few femtosecond) hard x-rays for XRD in the pump-probe scheme following shock loading [17].

But molecular dynamics (MD) also has a significant drawback. Simulations are limited in their space-time dimensions. Usually simulated condensed objects cannot be larger in volume than cubic micron and the duration of tracking of the evolution cannot be more than several tens of nanoseconds. G I Kanel' with coworkers systematically combines together data from small (10–100 nm) and large (mm) scales obtaining universal dependencies, see [6, figures 4 and 5] for Hugoniot elastic limit and for spall strength, respectively. We see from that, that the small scale MD data are not exception but they are continuation of the well-established mm-scale knowledge to the scales approaching to the ultimate theoretical strength-coupling between the mm-scale theories of plasticity and MD simulations.

In the previous classification (or ranging) there are three types of shock structures in solids: an elastic shock, a split elastic-plastic structure, and a plastic shock. The structures change each other as piston pressure p increases. A distance between the jumps increases in the case with a split elastic-plastic structure—the plastic shock moves slower than the elastic shock. Thus the split structure is a two-wave (2W) structure. The elastic shock is called a precursor, a weak precursor ahead the stronger plastic one.

Another regime of dynamic interaction between the elastic and plastic shocks was found in our MD simulations [8]. Let the plastic jump is continuously supported by a piston hold at permanent pressure p. Than thanks to interaction the plastic shock continuously supports the elastic front at a fixed distance d ahead. Value of this distance depends on value of pressure p. We call this structure the one wave (1W—because both jumps move together at the same speed) and two zone (2Z—because there are clearly defined and spatially separated elastic and plastic zones) wave—the 1W2Z shock for brevity.

Existence of the universal dependencies connecting atomic and macroscopic scales (they are mentioned above [6]) lead us to find traces of the regime 1W2Z at large space-time dimensions. Before the existence of the 1W2Z propagation regime was confirmed up to the separation distance $d = 200$–400 nm [8] due to resource limits imposed onto molecular dynamics simulations. The separation $d(p)$ increases as pressure decreases. How large it may be? The first part of the paper is devoted to this problem.

In the second part the peculiarities of the shock formation, its propagation, and evolution of solid transferred by the shock into a plastic state (evolution of solid after escape of a shock) are considered for subpicosecond ($\tau_\mathrm{L} \sim 0.1 \times 10^{-12}$ s) and nanosecond ($\tau_\mathrm{L} \sim 10^{-9}$ s) pulse durations.

A detailed description of the structure of the article and the purpose of individual sections 2–10 is given in concluding section 11.

2. Single entity: elastic compression as a first step of elastic-plastic transformation

Nonlinear acoustic disturbance propagates with a Mach number greater than one. The Hugoniot adiabatic curve starts from the initial point. Our initial point corresponds to uncompressed solid at room temperature. In an established (steady-state) state the disturbance generated by a piston supported by permanent pressure has to be a shock. The Hugoniot curves are shown in figure 1.

The yield stress Y elevates the plastic uniaxial compression above the hydrostatic one. This is because the initial elastic section is steeper than the plastic section. Difference between the curves "vol" and "pl" is $(2/3)\,Y$ in the model of elastic-plastic isotropic body [29]. Plastic speed of sound c_pl in the initial state defines the slope of curve "vol" near initial point in figure 1 (straight line *2*). While the elastic Hugoniot adiabat "el" concerns direct line *1* corresponding

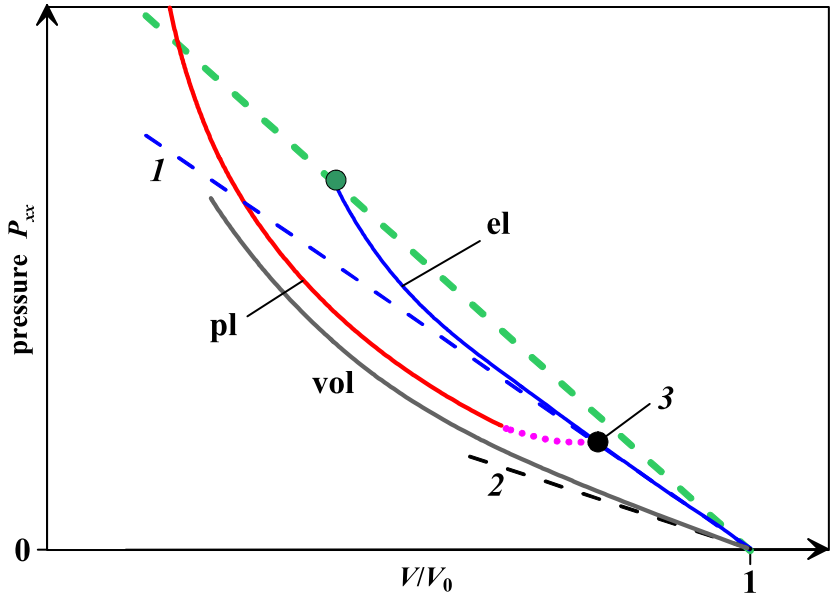

Figure 1. Comparison of hydrostatic (or volumetric—"vol" curve) and uniaxial compressions. "Volumetric" means homogeneous shrink along all three spatial axes. There are two types of the uniaxial compressions. One is the elastic ("el") while the second is plastic ("pl") compression. The "el" and "pl" stress curves relates to the corresponding Hugoniot curves. Elastic body is more rigid thus its Hugoniot is steeper. Initial volume is V_0. Speeds of elastic and plastic sounds are straights *1* and *2*, respectively; approximation of isotropic elastic-plastic body is considered. Black circle *3* indicates the Hugoniot elastic limit. The dotted piece of the "pl" Hugoniot corresponds to decaying plastic shocks observed in [11,27,28]. Although formally these shocks cannot be placed on the $p - V$ diagram because they are not stationary.

to the speed of elastic sound

$$c_{\rm el} = \sqrt{[B + (4/3)\,G]/\rho} = \sqrt{c_{\rm pl}^2 + (4/3)\,G/\rho} = c_{\rm pl}\sqrt{1 + (4/3)\,G/B}, \qquad (1)$$

where B and G are bulk and shear modulus.

2.1. Elastic shock

Let us consider the classification of the structures of shocks mentioned above. The first regime relates to a pure elastic shock (the 1W shock). It occupies the range of piston pressures p below the Hugoniot elastic limit: $0 < p < p_{\rm HEL}$. Corresponding Rayleigh line connects the initial point and the point belonging to the elastic Hugoniot curve "el" below the black circle *3* in figure 1; we will call this circle the usual Hugoniot elastic limit (HEL).

Pressure corresponding to circle *3* HEL in figure 1 is small relative to the bulk modulus. Therefore, the Hugoniot curve "el" in figure 1 is almost indistinguishable from the direct line *1* in this range of piston pressures. Regime with a single elastic shock is simple, apart from the fact that the limit HEL is a conditional value. As was said it is marked by circle *3* in figure 1.

According to papers by G I Kanel' with coworkers [6, 28, 30, 31], the value of HEL varies. For example, the value depends on the time (and vice versa) during which the uniaxial load σ_{xx} is maintained in elastic solid. There is a definite waiting time t for every value of the load σ_{xx} when the elastic solid of fixed length transits to a plastic state: $t(\sigma_{xx})$ and $\sigma_{xx}(t)$. There is connection between the value of HEL and the function $\sigma_{xx}(t)$. If t is time of propagation of

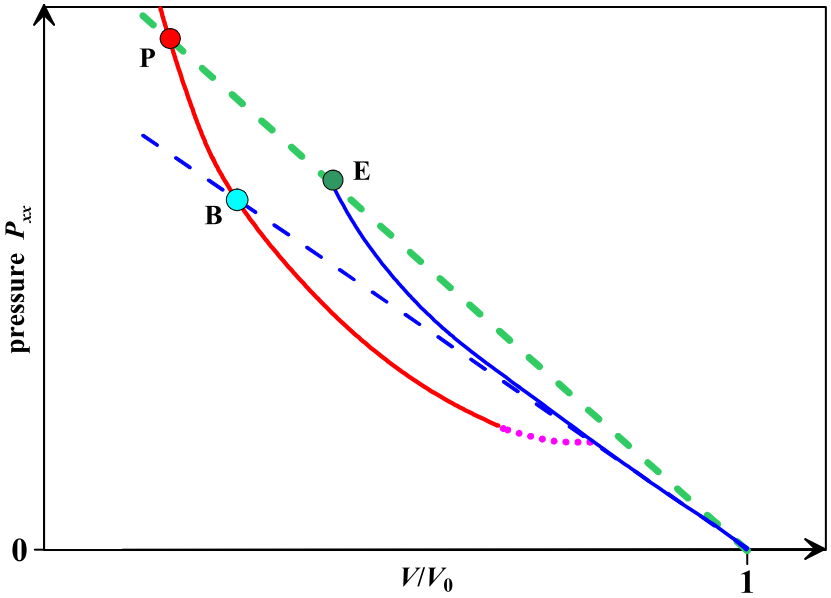

Figure 2. The elastic and plastic Hugoniots together with the two 1W2Z elastic plastic shocks. The shocks are presented by the Rayleigh lines 1–B and 1–E–P. The abbreviation 1W2Z means that there are two zones ("2Z": elastic 1–E and plastic E–P) in the internal structure of the single wave. The wave is single ("1W") because it moves as whole: both segments 1–E and E–P have equal slopes since they belong to the single Rayleigh line. As it is known, the slope defines propagation velocity.

an elastic shock started in time $t = 0$ and carrying the load $\sigma_{xx}(t)$ then we can write $x = c_{\rm el}\, t$ instead of t in $\sigma_{xx}(x)$.

Considering the regime with a single elastic shock wave, we assume that the piston is driven by permanent pressure p below the $p_{\rm HEL}$ shown in figure 1. The value $p_{\rm HEL}$ gradually decreases with time as $\sigma_{xx}(x)$. Thus if we wait enough then the elastic shock passes distance $x = c_{\rm el}t$ and if the value of HEL $p_{\rm HEL}(x)$ decreases below the piston pressure p then our purely elastic shock (covering all space between a piston and a shock front) finishes and the flow transits from the first regime with a single elastic shock to the split regime—the second regime according to the standard classification given above in Introduction. After the transition a plastic shock begins to propagate from a piston and behind the elastic shock.

2.2. A family of the single wave elastic-plastic shocks

As was said above, the boundary $p_{\rm HEL}$ of the pressure p on the piston between the elastic shock regime and the split elastic-plastic regime is not strictly defined; the split regime was defined in section 1 above (Introduction). We better understand the meaning of the split regime, if we first consider the 1W2Z regime. The examples of the 1W2Z regimes are shown in figure 2.

The 1W2Z shocks form an one-parametric family. Some selected 1W2Z shock from a 1W2Z family of shocks is defined or by its particular propagation velocity, or by its piston pressure p. The separation distance $d(p)$ between the elastic and plastic shocks inside the particular 1W2Z structure depends on pressure p. The distance decreases as the pressure p increases.

The upper limiting 1W2Z wave corresponds to the upper value of the pressure $p_{\rm up}$. At this pressure the distance d decreases down to the interatomic distance. Thus for the even higher pressures $p > p_{\rm up}$ only the pure plastic regime exists. For aluminum the values $p_{\rm up}$ are somewhere in the range 40–65 GPa depending on the state of metal inflowing into a shock structure [8].

2.3. The weakest 1W2Z wave

Figure 2 shows the 1W2Z wave family. The upper edge (wave of higher intensity) of this family is easily defined, see previous subsection 2.2. How to define the bottom edge 1–B in figure 2?

Let us calculate velocity of a plastic shock from Hugoniot adiabatic curve (from the Rankine–Hugoniot relations which follow from conservation laws). It is known that up to very strong shocks the Hugoniot curve is well approximated by the so called "us-up" relation. For a plastic shock this relation is

$$u_{\rm s} = c_{\rm pl} + a_{\rm pl}\, u_{\rm p}, \tag{2}$$

where $u_{\rm s}$ is shock velocity, $a_{\rm pl}$ is dimensionless coefficient $\simeq 1$, and $u_{\rm p}$ is velocity of a piston in the frame where material is at rest ahead to the shock front. Material comes to a shock with velocity $u_{\rm s}$ and passes in with velocity $u_{\rm s} - u_{\rm p}$ in the reference frame propagating together with a front.

For aluminum the coefficients (2) are $c_{\rm pl} = 5.35$ km/s, $a_{\rm pl} = 1.37$, see, e.g., [7, 8]. Velocity of a plastic shock $u_{\rm s}|_{\rm pl}|_{\rm crit}$ corresponding to the 1W2Z wave limiting the family from the bottom side is equal to the elastic speed of sound:

$$u_{\rm s}|_{\rm pl}|_{\rm crit} = c_{\rm el}. \tag{3}$$

Condition (3) corresponds to the Rayleigh line 1–B in figure 2.

For aluminum an elastic speed of sound $c_{\rm el}$ is ≈ 6.5 km/s. Then from equation (2) we obtain

$$u_{\rm p}|_{\rm pl}|_{\rm crit} = (c_{\rm el} - c_{\rm pl})/a_{\rm pl} = 0.84{\rm km/s}. \tag{4}$$

This is the slowest piston still supporting the weakest 1W2Z wave.

Knowing piston velocity (4) we can find corresponding compression $(V/V_0)|_{\rm pl}|_{\rm crit}$ behind the plastic shock wave. The expression for compression follows from kinematic conditions and conservation of mass $\rho_0 u_{\rm s} = \rho(u_{\rm s} - u_{\rm p})$. The expression for the critical compression is

$$(V/V_0)|_{\rm pl}|_{\rm crit} = 1 - u/(c_{\rm pl} + a_{\rm pl}\, u) = 0.87, \tag{5}$$

where u is $u_{\rm p}|_{\rm pl}|_{\rm crit}$ (4).

Corresponding critical pressure is defined by the value of (5) and the momentum conservation law. This pressure is

$$p_{\rm crit} = \rho_0\, c_{\rm pl}^2\, \frac{1 - V/V_0}{[1 - a_{\rm pl}\,(1 - V/V_0)]^2} = (1/a_{\rm pl})\rho_0\, c_{\rm el}\,(c_{\rm el} - c_{\rm pl}) = 14.7\,{\rm GPa}, \tag{6}$$

where V/V_0 is given by expression (5). The pressure (6) is the pressure at a piston in the point B in figure 2. This is the pressure in a plastically compressed aluminum behind a plastic front. Previously point (4), (5), (6) was called the overdriven point.

It is difficult to estimate the distance d between the jumps for the plastic compression (5) and plastic pressure (6). But we suggest that it is very significantly larger than the micron scales achieved in MD simulations [8]. Indeed, according to figure 2 for the bottom end of the one-parametric family with the Rayleigh line 1–B the pressure behind the elastic shock is somewhere near the traditional values for the Hugoniot elastic limit. That is, it is small, less than 1 GPa for aluminum. Then a shear stress behind such elastic shock uniaxially compressing aluminum is rather small. Then a degree of metastability is small. This means that aluminum may survive in such states much longer than in MD simulations [8] where degree of metastability is higher.

2.4. The split regime

The split regime obviously appears for piston pressures below the limiting value (6). Velocity of a plastic front decreases below the elastic speed of sound. So the plastic wave starts lag behind the elastic wave.

The elastic wave loses dynamic support from the side of the plastic wave, as the distance between these two jumps increases. The plastic shock is permanently driven by a constant piston pressure. Therefore, a pressure field behind the plastic front is homogeneous.

While the elastic front escaping from support decays thank to its nonlinear stretching. The elastic shock transits to a triangular shape. The triangular becomes wider and wider because of weak but finite nonlinear effects: dependence of speed of sound on amplitude—dispersive weakening. This is a picture with asymptotically dynamically unrelated objects: plastic and elastic fronts.

Although usually a different picture is drawn. In the usual picture there are two Rayleigh lines with different slopes. The kink between these lines is supported by point *3* (traditional Hugoniot elastic limit) in figure 1 above, see, e.g., [32]. But slowly point *3* decreases along the elastic Hugoniot. Thus, outwardly, both pictures become similar.

While in the 1W2Z case the elastic and plastic shock waves are dynamically connected. Their separation distance d fluctuates near the average value $d(p)$ depending on a piston pressure. There are two types of disturbances causing the fluctuations. In the first type the delay of elastic-plastic transformation near the plastic front pushes elastic front because untransformed elastic metal have larger volume than transformed one. The delayed transition sends a triangular elastic waves propagating from plastic to elastic front [8]. Flow behind an elastic shock is subsonic relative to elastic speed of sound. Therefore, the triangular waves catch up with the elastic front and throw it forward.

In the second variant of this dynamic connection, a layer of a uniaxially elastically compressed crystal experiences a collapse from time to time [32, 33]. The collapse shrinks thickness of this layer due to additional compression of metal around the nucleus of destruction. The places and moments when a specific collapse begins are controlled by a probabilistic process. Usually they take place more close to the plastic shock. In this case the piece of the elastically compressed crystal is longer hold under load. Two rarefaction waves run away from the place of collapse. This process decreases slightly too high longitudinal stress at the elastic front thus adjusting an elastic load to corresponding piston pressure.

The picture of the transverse interaction of the collapse points is extremely interesting [32,33]. Three-dimensional phenomena are also very beautiful in the first variant with elastic-plastic transformation near the plastic front [8, 14, 15].

The proposed classification of the shock structures is as follows:

- Firstly, simple, purely elastic shock waves.
- Secondly, split waves.
- Thirdly, the 1W2Z single-wave mode.
- Finally, fourthly, simple purely plastic shock waves.

This classification includes regime 1W2Z.

If we suppose that the Hugoniot Elastic Limit (HEL) decreases with time, then all shocks from split regime will go into 1W2Z regime, if we wait for the required long time. That is, there will be a gradual straightening of two segments of the Rayleigh lines into one common segment as the HEL moves down to its final position.

3. Peculiarities of picosecond laser loading of solids

3.1. General peculiarities

Often a laser is used as a tool for loading of a solid; let us mention in this connection, e.g., using of lasers for studies of equation of state [18]. But this tool has its own very specific features. The tool causes heating of an absorbing surface layer. Thickness of a heated layer d_{T} is defined by a light penetration depth in an absorbing matter (a skin-layer in metals for optical radiation) and thermal conductivity.

Strong load means intense heating. Thus, the phenomena of melting and evaporation become significant. The characteristics associated with melting and evaporation are well known. There is an additional feature linked specially to lasers with ultrashort pulse. This is a pronounced mechanical action of such a pulse.

Let us define the term "ultrashort pulse". The pulse is ultrashort if its duration $\tau_{\rm L}$ is less than acoustic time scale $t_{\rm s} = d_{\rm T}/c_{\rm s}$. Then the hydrodynamic unloading is delayed relative to the duration of the period of time $\tau_{\rm L}$ for which the heating takes place. After such laser pulse matter unloads under pressure $p \approx \Gamma E$, where $\Gamma \approx 2$ is Gruneisen parameter, $E \approx F_{\rm abs}/d_{\rm T}$ is volume density of absorbed energy, $F_{\rm abs}$ is absorbed fluence. For example, $d_{\rm T} \simeq 100$ nm, $t_{\rm s} \simeq 20$ ps, $F_{\rm abs} \simeq 0.3$ J/cm^2, $p \simeq 60$ GPa.

A laser pulses of longer durations $\tau_{\rm L}$ also drive pressure, but less effectively: $p \sim (t_{\rm s}/\tau_{\rm L})\,\Gamma E$, (see details in next section 4).

Ultrashort pulse creates significant tensile stress. This is the main qualitative difference from the action of long pulses. Thus, long pulses can melt and evaporate the target material. While an ultrashort pulse can mechanically tear off a layer of matter in the irradiation spot.

This phenomenon is called spallation or cavitation. It explains formation of the Newton rings [34,35]. Spallation develops after nucleation of voids [10,12,13,16]. The nucleation begins above the nucleation threshold $F_{\rm abs}|_{\rm nucl}$. For ultrashort laser pulse the nucleation and spallation take place in liquid phase—a surface layer melts before the nucleation.

Surface tension resists to expansion of voids. Therefore, the spallation (or ablation) threshold $F_{\rm abs}|_{\rm abl}$ is higher than the nucleation threshold $F_{\rm abs}|_{\rm nucl}$ [36, 37]. Capillary forces may be very significant increasing the threshold $F_{\rm abs}|_{\rm abl}$ approximately twice above the nucleation threshold $F_{\rm abs}|_{\rm nucl}$. Such large increase is observed in metals like Mo, Ta, Ni, Ru with a high coefficient of surface tension and thin heated layers $d_{\rm T}$; thermal conductivity is small therefore the layer $d_{\rm T}$ is thin. Inertia of a thin layer is small thus surface tension is more effective in deceleration of these layers.

A prominent rim surrounds the laser spot [37]. Its position corresponds to the intermediate range of absorbed energies $F_{\rm abs}|_{\rm nucl} < F_{\rm abs} < F_{\rm abs}|_{\rm abl}$. In this range a nucleation takes place but the surface layer retains its mechanical connection with the target. Thus a porous surface layer appears [37].

Surface structures appear due to competition between inertia-capillary dynamics and cooling–freezing thermal processes. Subtle effects take place depending on the relationship between mechanical and thermal factors. Common shell covers the laser spot. The shell is in motion. For rather large spots (few tens of microns) the shell at an initial stage is composed from many individual shells covering their particular expanding bubble (every particular bubble is a product of expansion and merging of the small nucleus). Every individual shell is separated from its neighbor shells by a membrane.

If freezing is rather slow, then the separation membranes under common shell have time to break. Then the well defined wall is formed around the spot [38]. But in the opposite case, with high thermal conductivity and a thin liquid layer under the bottoms of the bubbles, the separation membranes remain frozen. These frozen membranes form a random edge of a spot.

3.2. Formation of frozen nanocavities and residual stresses

Figure 3 presents the final structures located near frontal free surface; laser acts to the frontal surface. Final means that this picture corresponds to late time after finishing of a pulse. At that late stage the structures are totally crystallized. Cavities are frozen into solid surrounding, compare with simulations and experiments in [37]. Pulse duration is $\tau_{\rm L} = 1$ ps. The time shown in figure 3 is 0.6 ns.

Aluminum film with dimensions $500\times500\times24$ nm^3 was considered in this MD-MC simulation; MD means molecular dynamics; MC is Monte-Carlo subroutine describing electron thermal

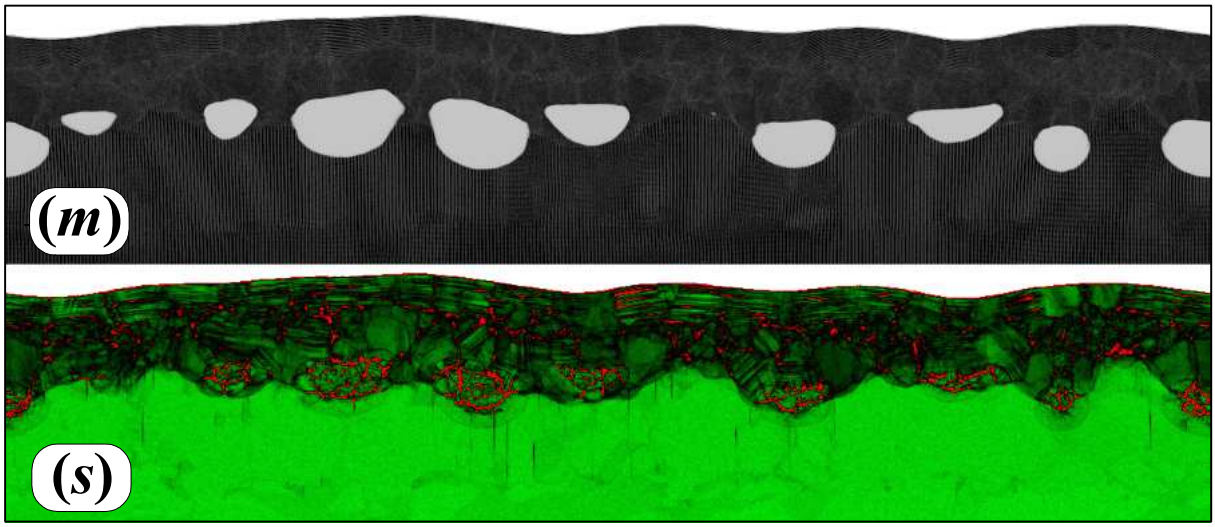

Figure 3. Frozen nano-structures that remained in a thin subsurface layer after exposure to a picosecond laser pulse are shown. The upper panel (m) gives density distribution. The bottom panel (S) demonstrates distribution of a symmetry factor S. The factor shows local order of a crystalline lattice. Green colors correspond to a solid state. Regions colored with deep green shows nano-crystalline aluminum. We are interested in the residual deformations produced in a target by an ultrashort laser pulse. From this point of view, melting, nucleation and freezing of nano-cavities is a side effect. The horizontal dimension is 0.5 micron.

conductivity of aluminum. Electron thermal conductivity is high. It cools down a hot surface layer. Therefore, the liquid phase freezes. In simulation shown in figures 3–6 357 million atoms were used. The simulation box is bounded by periodic boundary conditions in the transverse directions. Absorbed fluence of 70 mJ/cm^2 is below the ablation threshold $F_{\rm abs}|_{\rm abl}$ but above the nucleation threshold $F_{\rm abs}|_{\rm nucl}$.

Residual dislocations are clearly visible under the layer of frozen bubbles in figure 3. They are formed by combined action of shock compression and thermomechanical stress field. Deep green colors around the frozen bubbles show the nano-crystallin aluminum.

Distributions of pressure and temperature in the longitudinal direction at the early stage is shown in figure 4. We see the shock propagating from left to right. The shock is formed after breaking (turnover) of a compression wave created by supersonic heating. We call the heating supersonic because duration of a heating pulse $\tau_{\rm L} = 1$ ps is much less than acoustic time scale $t_{\rm s} = d_{\rm T}/c_{\rm s} \approx 20$ ps. This is connected with superfast expansion of absorbed heat from a skin-layer to the heat affected zone $d_{\rm T} \approx 100$–120 nm. Just few picosecond $t_{\rm T}$ are necessary to create the layer $d_{\rm T}$. The speed $d_{\rm T}/t_{\rm T}$ of expansion of internal energy from a skin during forming the layer $d_{\rm T}$ is ≈ 7–10 times higher than speed of sound in aluminum.

Reflection of a compression wave from a free surface produces a back part of a wave. This part is carrying a tensile stress inside a target, see figure 4. At the instant shown in figure 4 the tensile part has a trace of a spallation shock. This shock forms when molten aluminum begins to nucleate. The liquid layer is shown in figure 4. The deep well in the density profile shown in figure 5 is the consequence of formation of bubbles.

Pressures are moderate, but significantly below a bulk modulus of aluminum. Therefore, compressions and expansions related to the compression and tensile part of pressure profile in figure 4 are weak at the density profile shown in figure 5. The shock weakly heats aluminum—see small temperature jump corresponding to the shock in figure 4.

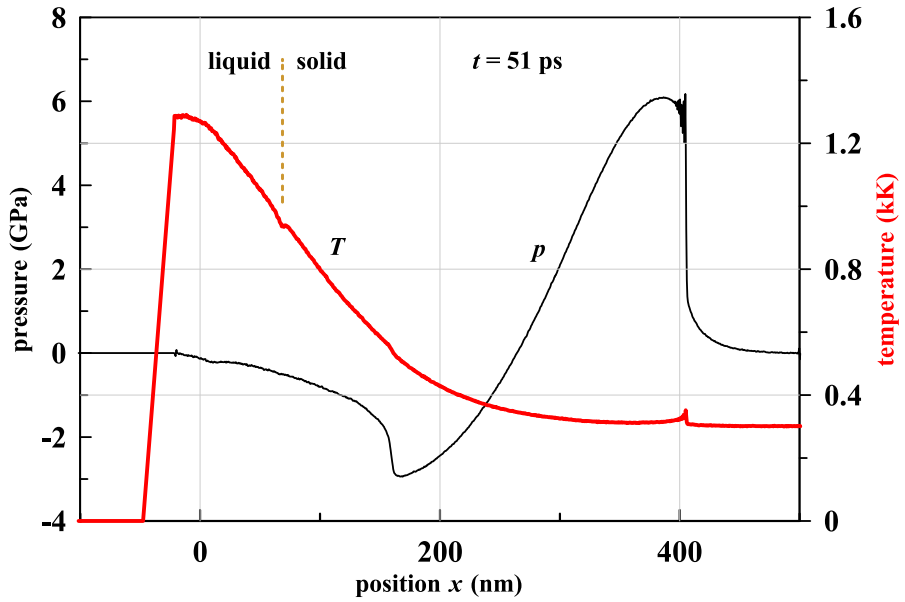

Figure 4. Distributions of pressure and temperature in the longitudinal direction at the early stage. At this stage the shock still is approaching the rear-side of a film. The distributions are obtained after averaging along the transverse directions relative to the vertical (longitudinal) direction. Laser beam comes from the left side. Before laser action, the boundary of the target with the vacuum is located at the point $x = 0$.

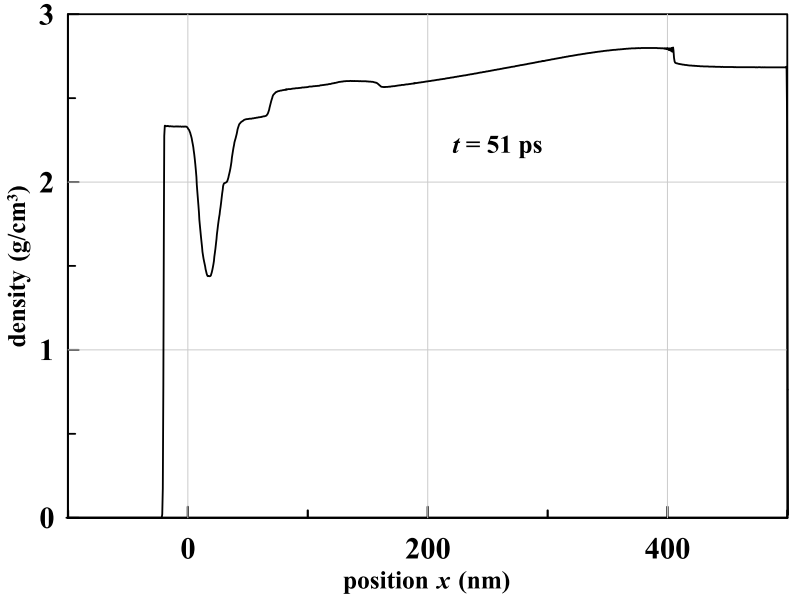

Figure 5. Density distribution along the longitudinal direction. This is the vertical direction in figure 3. The deep well at the left side near the free surface corresponds to the chain of bubbles. These bubbles nucleate due to action of the tensile part of the pressure profile shown in figure 4.

Final state of aluminum is shown in figures 3 and 6. We construct special boundary condition at the rear side of the film. This is the right side seen in figures 4–6. This condition leaves the shock seen in figure 4 through the right boundary without reflection.

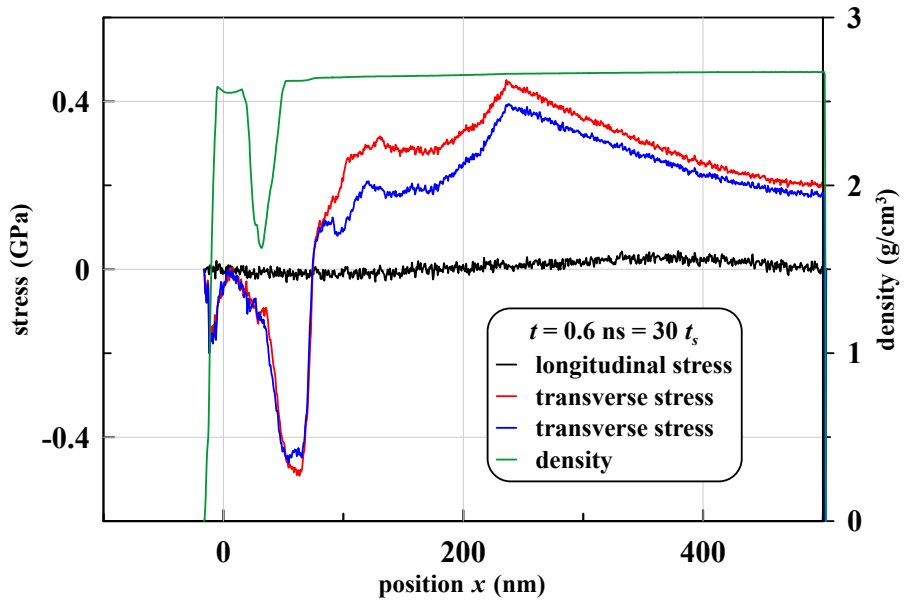

Figure 6. Final profiles are shown, corresponding to the late time instant 0.6 ns. Density and symmetry maps for this time are presented in figure 3. We see creation of significant residual stress field. It relates to the residual deformations shown in figure 3. Here pressure components p_{ii} are shown. The stress components are $\sigma_{ii} = -p_{ii}$.

Thus our simulation describes the case of an infinite target. In this target the acoustic profile shown in figure 4 travels to the bulk and loses its connection to the surface layer.

Aluminum in figures 3 and 6 cools down to temperature 400 K. This temperature is near the initial (prior to laser heating) temperature 300 K. Temperature gradient across the film is small, approximately 70 K.

We want to emphasize two remarkable features. The first is the frozen nanobubbles in a solid nanocrystalline matrix (under the surface). The second feature relates to the residual strain and stress fields. We clearly see the remaining fields in figures 3 and 6. They correspond to late enough time—the 30 acoustic time scales $t_s = 20$ ps.

Longitudinal stresses are close to zero: this is due to the unloading wave from the side of the free surface. But the transverse stresses survive at the level of few hundred MPa. A thin stressed layer is located near the bubbles; compare the density profile and the profiles of transverse stress in figure 6. It seems that this layer is connected with thermal processes around the bubbles. The deeper layer seems is formed due to plastic transformations under action of shock compression. The shock wave shown in figure 4 is Super-elastic one. We say “Super-elastic” shock, because it remains elastic at pressures that are much higher than the generally accepted values for elastic-plastic transformation HEL, see section 2. Thus formally aluminum should return to its unperturbed state after passing of shock.

At least in part, this transverse stress is formed due to, firstly, one-dimensional (1D) geometry, secondly, periodic boundary conditions and, thirdly, to the heating of our layer with a thickness of 0.5 microns. 1D geometry means that the illumination is uniform along the frontal surface of the target. That is, the diameter of the laser spot is much larger than the target thickness of 0.5 microns in the longitudinal direction. Periodic boundary conditions do not allow aluminum to expand in the lateral directions.

The boundary condition on the rear-side of our target allows you to release a shock wave from our layer without reflection on the rear-side border. Thus, our formulation reproduces the

situation with a bulk target. But the foregoing relates to the mechanics of the processes under consideration. Heat redistribution is limited by the rear-side border. The absorbed energy first spreads from the skin layer with a thickness of 20 nm and forms a heating layer with a thickness of approximately 100 nm. In the distant past, heat from a heating layer of 100 nm spreads over the entire target with a thickness of 500 nm. At the time point shown in figures 3 and 6, the average temperature in the layer is 470 K. The difference between the maximum and minimum temperatures is 150 K. The initial temperature was 300 K. To equalize the temperatures across the 500 nm layer, a time of the order of 1 ns is required.

4. Laser shock peening by nanosecond laser pulse

Laser action has long been used to generate shock waves in materials. The traditional branch of these applications is to clarify the equations of state (EOSs) at high energy densities that are unattainable with chemical explosives [18]. The other branch is connected with the modern technology of laser peening. By peening, the wear (fatigue failure) and corrosion resistance is greatly (tens, hundreds of percent [39]) increased. For example, using laser peening to strengthen the details of aircraft engines—see [40] and [41].

In this paper, we want to draw attention to significant common phenomena for such different technologies as laser shock peening (LSP) and laser ablation in liquid (LAL). At the same time, scientific communities for LSP and for LAL to a large extent have no scientific connections with each other. The same data is interpreted differently. In peening experiments, crater formation is associated with residual plastic deformations (ablation is neglected), see, for example, [42]. Whereas in experiments with ablation, it is believed that a crater is formed due to the entrainment of a substance into a liquid [43], that is the mechanics of the deformation of a solid below the surface of the crater is neglected. Meanwhile, the pulse duration of the order of nanoseconds and comparable intensities of 1–10 GW/cm^2 are used in both technologies. To increase the number of produced nanoparticles in LAL and enhance residual deformations in LSP, the laser pulse energy is increased to values limited by the threshold of optical breakdown of the liquid. The aluminum target was used in [42], while [43] considered a corundum target; the deformation of brittle materials, which include corundum, is difficult [44].

Of course, understanding the physics of the phenomena occurring is essential for successful work. In many ways, this understanding is based on analytical solutions that are complemented by numerical calculations. In the introductory part of this paper, we turn our attention to analytics related to the ablation into water and peening problems. These analytical solutions describe the expansion into vacuum and condensed matter, long and short pulses. Below is a short list of solutions. In the 70–90s of the XX-th century, a detailed analytical theory of the plasma laser corona was developed in the approximation of a stationary flow and a fixed degree of ionization [45, 46]. This solution considers the expansion of the substance in the corona into a vacuum; the energy absorbed in the region of critical density is transmitted by the electronic thermal conductivity to the ablation front, which moves subsonically into a relatively cold dense substance.

In the case of ultrashort laser pulses (USLP, there is no transition to a stationary flow) and–or during the expansion into a condensed (not vacuum and not gas) environment, the analysis, of course, changes qualitatively (compared to the plasma corona). A simple thermo-acoustic solution to help the understanding and implementation of the first estimates, for the case of the impact of USLP on thin films is given in [47]; thin film is considered, the laser warm-up time of which $t_\mathrm{T} \sim d_\mathrm{f}^2/4\chi$ throughout the thickness is less that the time $t_\mathrm{s} = d_\mathrm{f}/c_\mathrm{s}$, for which the sound runs through the thickness; duration of τ_L of the pulse is small $\tau_\mathrm{L} < t_\mathrm{T}$; here and below d_f is the film thickness, χ is the thermal diffusivity of the film, c_s is the speed of sound.

The analytical approach in the case of USLP and ablation into the liquid [48] is based on the classical solution of the problem of the decay of an arbitrary discontinuity (Riemann problem):

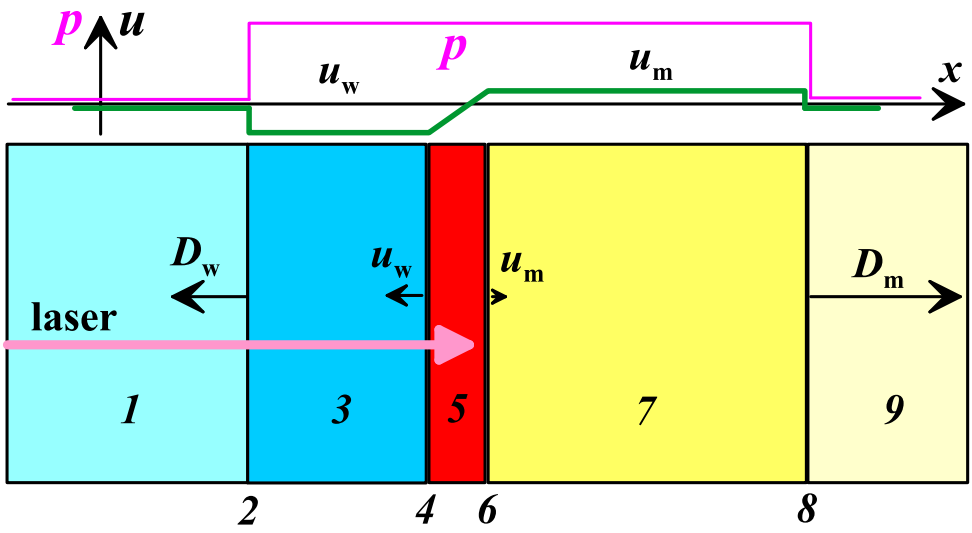

Figure 7. Laser heating of a metal target through water. Main ideas of the model developed in [49] are presented. The laser passes through unperturbed water *1*, crosses the shock wave front *2*, passes through the shock-compressed water *3* and is absorbed in the hot metal layer *5*. The pulse is long in time ("subsonic" heating) in the sense that the sound scale L/c_s is much shorter than the pulse duration τ_L, here L is the width of layer *5*. Therefore, boundaries *4* and *6* of layer *5* act as two subsonic pistons pushing waves *2* and *8*. Waves *2* and *8* propagate much faster than the expansion rate of layer *5*. So, layer *5* is thin compared with layers *3* and *7*.

for $t < 0$, we have two half-spaces in contact with each other; for $t = 0$, the separating wall is removed. Substances in half-spaces have different pressure values and, at $t < 0$, they are at rest. In the case of long pulses $\tau_L \gg d_T/c_s$, the analysis of heating of an absorbing target through a transparent dielectric is completely different [49], here d_T is the thickness of the heating layer. Figure 7 presents a diagram of the corresponding processes.

Below we describe this diagram in detail and compare it with the results of our calculations. Due to our analysis, new information important for LSP and LAL technologies will be obtained. For example, it turns out that the formula for $p \propto \sqrt{I(t)}$ from [49], which predicts a pressure drop to zero in layer *5* in figure 7, does not work at the end of the laser pulse and later in time. Here $I(t)$ is intensity of a laser pulse. In fact, the pressure decreases to a finite value when $I(t) \to 0$. This finite value is determined by the pressure of the hot metal in layer *5*. Evolution in time of this pressure is defined by evolution of degree of expansion of hot metal.

5. On the heating layer supporting nonlinear acoustic waves

Figure 7 shows a wide area of acoustic perturbation from x_2 to x_8. It is created by a long-lasting laser pulse. The width of $x_8 - x_2$ is approximately $(c_w + c_m)(t - t_{ini})$. The time t will be counted from the maximum of the laser pulse with a Gaussian profile $I(t) = I_0 \exp(-t^2/\tau_L^2)$. The moment of the pulse in numerical calculation denote t_{ini}; we have $t_{ini} = -3\tau_L$.

Sound velocities in water and metal are denoted by c_w and c_m. For absorbable intensities $I_{abs} \sim 1$ GW/cm^2 and durations $\tau_L \sim 1$ ns the pressure to the end of the pulse of the order of 1 GPa. These pressures are small compared to the bulk metal module $B_m \sim 10^2$ GPa and of the order of the water module $B_w = 1.5$ GPa. Therefore, the acoustic perturbation running through the water in figure 7, is moderately nonlinear and weakly nonlinear in metal.

The pistons *4* and *6* create a simple Riemann waves in water and metal, correspondingly. Focusing of characteristics and breaking of the Riemann wave is happening in the water early

due to the high nonlinearity of the waves in the water. In the linear acoustic approximation, the pressure and velocity are connected via the acoustic impedance $p = zu$. In the model [49], the pressure is uniform over the interval from x_2 to x_8, see the graph in the upper part of figure 7. Then the water velocities u_w and metal u_m are homogeneous, each in its own domain, that is in *3* and *7*. The expansion rate of the hot layer is $\dot{L} = (1/z_\mathrm{w} + 1/z_\mathrm{m})p$. In the numerical calculations below, we consider a pair of gold and water. Acoustic impedance of water is small: $z_\mathrm{w} \ll z_\mathrm{m}$. So $\dot{L} \approx p/z_\mathrm{w}$.

The above relation $\dot{L} = p/z_\mathrm{w}$ follows from the acoustic approximation. A difficult place is to establish a balance of energy. Energy supply to the hot layer *5* (arrow "laser" in figure 7), firstly, heats the substance of the layer and, secondly, transfers energy to acoustic waves in water and metal. In [49] this balance is written as

$$I - p\dot{L} = (\mathrm{d}/\mathrm{d}t)(E_\mathrm{int}L). \tag{7}$$

That is, the intensity absorbed in the layer minus the mechanical work of the pistons is spent on increasing the internal energy E_int of layer *5*. In this case, it is assumed that new portions of the substance do not enter layer *5*; that is layer *5* is created at an early stage, and then its mass does not change. It is necessary to link the energy E_int and the pressure p, generated by heating in layer *5*. Then the equation (7) will allow us to express the pressure p through the intensity I.

In model [49], the following assumptions are made. The internal energy E_int consists of two terms: $E_\mathrm{int} = E_\mathrm{T} + E_\mathrm{ion}$, where $E_\mathrm{T} = \alpha E_\mathrm{int}$ is the thermal energy that determines the pressure of p, and $E_\mathrm{ion} = (1-\alpha)E_\mathrm{int}$ is the energy that is spent on the ionization of the substance in layer *5* and is not involved in the pressure increase p. Thus, the effective increase of heat capacity during ionization is taken into account. It is assumed that the coefficient α is constant. In addition, it is assumed that $p = (2/3)E_\mathrm{T}$, as in the case of a monatomic ideal gas. Under these assumptions, for a constant laser pulse we obtain

$$p = \sqrt{\frac{2\alpha}{2\alpha+3} z_\mathrm{w} I} = p_1 \sqrt{\frac{\alpha}{2\alpha+3}} \sqrt{\frac{I}{I_1}}, \tag{8}$$

$$u_\mathrm{w} = \frac{p}{z_\mathrm{w}} = u_1 \sqrt{\frac{\alpha}{2\alpha+3}} \sqrt{\frac{I}{I_1}}. \tag{9}$$

Here z_w is the water impedance; $p_1 = 5.5$ GPa, $u_1 = 3.7$ km/s, $I_1 = 1$ GW/cm^2. If we put our values in numerical estimates (8, 9) then velocity $u_\mathrm{w} = 1$ km/s is obtained. So during the time of the order of $\tau_\mathrm{L} \sim 1$ ns the hot layer will expand to the thickness $L \sim 1$ μm. According to [49], the coefficient α is small (~ 0.1), and therefore significant.

6. Heating, expansion and acoustic radiation: the role of melting

We present the results of the numerical solution of the problem described by the approximate analytical model in the previous section. Consider a gold–water pair. Laser radiation passes through water and is absorbed in gold. The corresponding code was described in [47, 48], see also [50–54]. The pulse shape has the form $I = I_0 \exp(-t^2/\tau_\mathrm{L}^2)$, $\tau_\mathrm{L} = 0.5$ ns, the absorbed energy is 0.9 J/cm^2.

The flow in its development goes through a number of stages. The first is stage I, where the solid metal is heated. This stage ends when the melting of the metal begins. This is followed by stage II, in which the melt layer expands, and its temperature on contact with water increases. At the end of stage II, the temperature of the metal on the contact reaches a critical temperature of gold. In stage III, a gaseous layer of metal is formed near the contact. Stage IV refers to the end of the heating pulse. At this stage, a deep dip in the pressure profile begins to form. This dip is in the contact area. The appearance of the dip is due to the termination of heating of

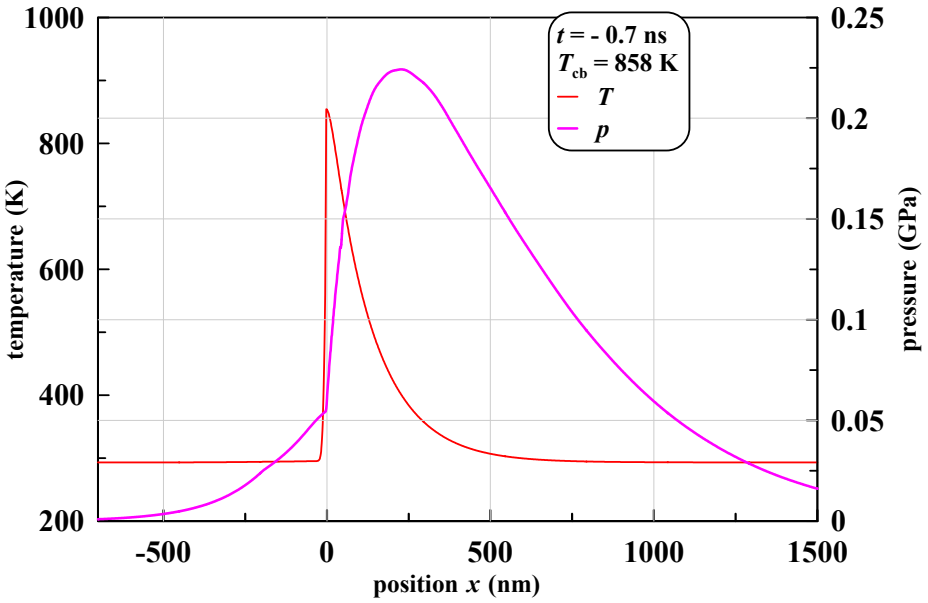

Figure 8. The situation at stage I that is before melting. The calculation is started at $t_{\rm ini} = -1.5$ ns. At this point, gold is to the right of the plane $x = 0$, and water is to the left. The initial temperature of water and gold $T_{\rm rt} = 300$ K. The heat spreads to gold at a depth of $d_{\rm T} = 0.1$ μm. In the plane at a depth of $d_{\rm T}$ the temperature is $(T_{\max} - T_{\rm rt})/2 + T_{\rm rt} = (T_{\max} + T_{\rm rt})/2$, that is $d_{\rm T} = 0.1$ μm is the full width at half-height by temperature increase. The pressure profile has smooth acoustic wings on the left and right.

the contact area (layer *5*) and due to escaping of the acoustic perturbations (continually formed during the action of the laser pulse) from the layer *5* in figure 7.

Let us illustrate the above with respect to the stages of the process. Let us start with stage I and its transition to stage II. Figure 8 shows the instantaneous temperature and pressure profiles shortly before the end of the stage I—the laser heats the metal, but the metal temperature remains below the melting temperature, for gold $T_{\rm m} = 1337$ K. The thickness of the heated layer of metal $d_{\rm T} = 0.1$ μm. If we estimate this thickness by the formula $2\sqrt{\chi(t_{\rm obs} - t_{\rm ini})}$, we get about 0.7 μm; here $\chi \approx 1.2$ cm^2/c is the coefficient of thermal diffusivity of solid gold, $t_{\rm obs} = -0.7$ ps is the point in time that figure 8 corresponds to. The value $t_{\rm ini} = -1.5$ ns—is the time when the code starts to work. It is clear that the estimate of $2\sqrt{\chi\,\Delta t}$ does not work, because the wing of the time intensity distribution $I \propto \exp(-t^2/\tau_{\rm L}^2)$ is very weak in the time interval near the moment of the beginning of the calculation $t_{\rm ini}$. Indeed, if $t_{\rm ini}$ is carried away to minus infinity, then this estimate will give an infinite thickness of the heated region, whereas the profiles in figure 8 practically will not change.

Pressure profile in figure 8 has smooth spatial wings on the left in water and on the right in gold. These are acoustic perturbations associated with the time-axis left wing of the time profile of the laser pulse $I \propto \exp(-t^2/\tau_{\rm L}^2)$, on which the intensity increases with time. Perturbations propagate along the characteristics with speed of sound in water and the gold from the layer heating. The laser energy is absorbed in the skin layer of the metal near the gold–water contact boundary. Acoustic disturbances are created due to temperature growth and thermal expansion of the substance in the heated layer with the current thickness of the order of $d_{\rm T}$.

The contact boundary reaches the melting temperature $T_{\rm m}$ at the time instant $t \approx -0.6$ ns (figures 9 and also 10 and 11); to better understand the melting, the phase diagram of gold is shown in figures 10, 11. Formation of a tooth on a pressure profile in figure 9 associated with the

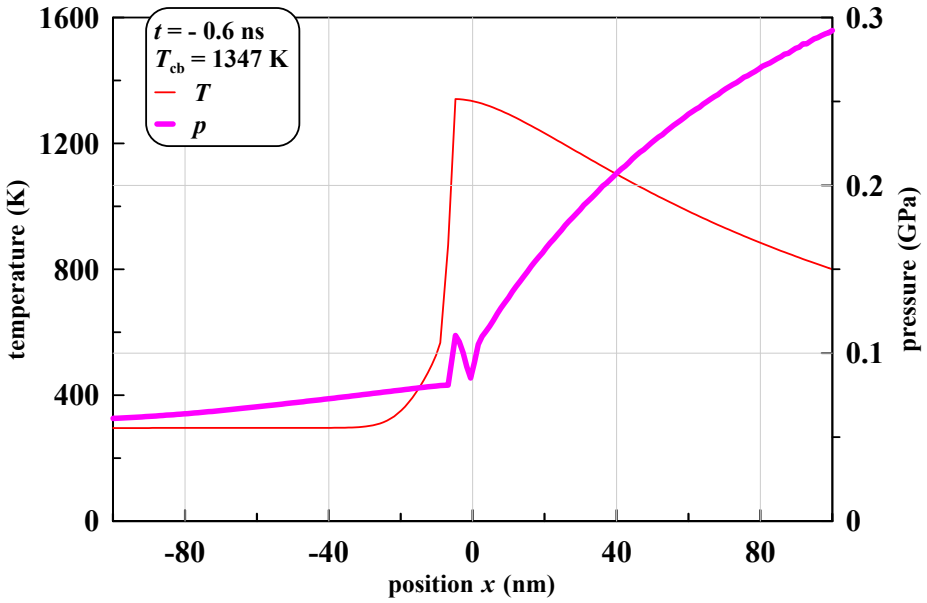

Figure 9. Beginning of stage II with a layer of melt. The contact temperature $T_{\rm cb} = 1347$ K by 5 degrees surpassed the melting point $T_{\rm m}(p)$ of gold under a pressure of 943 bar in the region of the contact boundary (cb). The dependence of $T_{\rm m}(p)$ is shown in the following two figures. At the moment of formation of the liquid phase, a tooth is formed on the pressure profile p in the contact area. At stage I, the p profile is smooth everywhere—there are no teeth anywhere.

appearance of the liquid phase and with the numerical difference scheme used in our computer simulation code. Outside the tooth, the pressure profile remains smooth, see figure 12.

A similar detail with profile strengthening due to the beginning of melting was observed earlier in works [61, figures 6 and 7], [62, figures 2 and 3] (melting imprint in the profile of a simple Riemann wave profile), [63]. All these articles are devoted to ultrashort laser pulses (USLP) when heating occurs isochorically. Then the melting section between solidus and liquidus is imprinted in the profiles of temperature and pressure. Then this imprint begins to travel along acoustic characteristics.

In [11], there is also observed the strengthening of the Riemann simple wave profile, which (strengthening) is emitted from the melting front when the melting zone is switched from supersonic to subsonic propagation. If the works [61–63] are based on the hydrodynamic code, then [11] is used molecular dynamics (MD). In MD, melting proceeds as in nature. The MD automatically takes into account the possible real effects of the melting nonequilibrium; in hydrodynamic modeling there is no disequilibrium, an equilibrium equation of state is used. In the MD pressure profiles, the melting site is smoothed, but remains noticeable. And if in [61–63] the plastic equation of state of matter in the solid phase is used (there are no elastic shock waves) [55–60], then MD [2,5,7–9,11,32,64,65] clearly shows the elastic-plastic transition; a detailed experimental and theoretical studies of elastic-plastic transition in ultrashort loading were carried out in the works of Ashitkov, Kanel, Agranat *et al* [6,66,67], see also [68,69]. It turns out [11], that there is a superposition of two effects (A) of the ablation imprint of melting on the characteristics and (B) of the formation of an elastic shock wave. The strengthening of the acoustic profile section by melting accelerates the formation of an elastic shock wave—the simple Riemann wave is tilted earlier because of the presence of a steeper section of pressure dependence on thermodynamic parameters in the melting region of phase diagram of equation of state (the strip between solidus and liquidus).

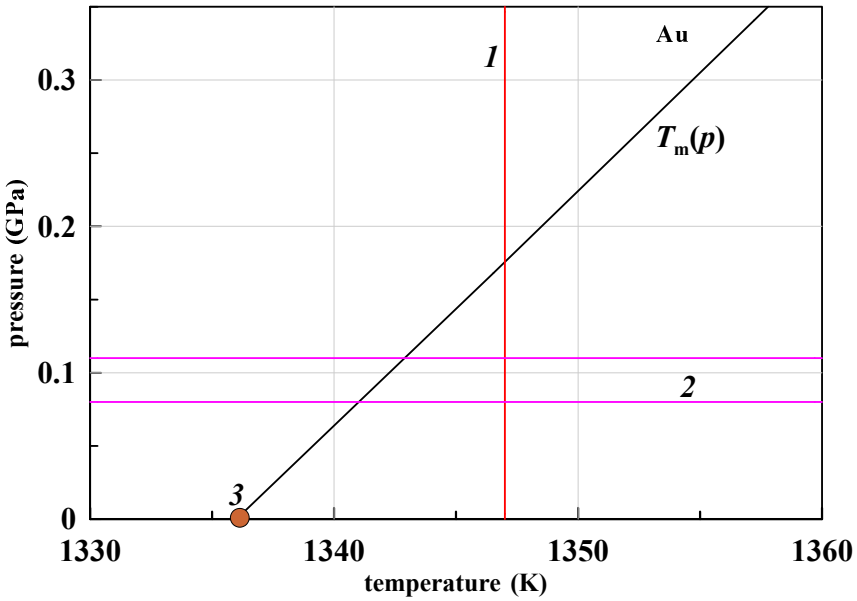

Figure 10. A small segment of the melting curve on the T–p plane of Au is presented. This is the segment near the triple point marked with marker *3*. A more complete phase diagram in the pressure range of interest is shown in the following figure 11. At the triple point, the melting point of gold (Au) is 1337 K. The lower and upper amplitudes of the tooth pressure, taken from figure 9, is shown here by two lines *2*. Contact temperature $T_{\rm cb} = 1347$ K in figure 9 is marked here by the vertical line *1*. This temperature corresponds to the time $t = -0.6$ ns. As you can see, the temperature $T_{\rm cb} = 1347$ K is 5 degrees higher than the melting point $T_{\rm m}|_{(p=943\ \rm bar)} = 1342$ K. The pressure of 943 bar corresponds to the average pressure between the two horizontal lines *2*.

Figure 13 shows the density, temperature and pressure profiles at the time instant $t = -0.2$ ns. At this point, the gold absorbed 29% of the laser pulse energy, that is 29% of 0.9 J/cm^2. The thickness of the gold melt layer in figure 13 is 0.25 μm. At stage II, shown in figure 13, the laser continues actively heat gold in the heating layer $d_{\rm T}$. This heating increases pressure in the layer $d_{\rm T}$. Therefore, the pressure profile has the form of a bump with a maximum shifted to the right of the heating layer $d_{\rm T}$. On the right and left acoustic wings a trace from the beginning of melting is clearly visible. The specified trace (or imprint), as discussed above for ultrashort pulses, has the form of a section with a steeper pressure stroke.

Oscillations running to the right and to the left of the melting front are associated with the error of the numerical difference scheme. Oscillations propagate along the characteristics. The calculation uses a one-dimensional hydrodynamic code with division into steps (cells) at the Lagrangian coordinate x^0, see [47, 48, 50–54]. The partition pitch (the length of the Lagrangian cell) is Δx^0 uniform over the integration interval. In the described calculation, $\Delta x^0 = 1$ nm is used. The time step is of the order of 0.1 fs. The velocity of the melting front relative to matter is $u_{\rm m} = 400$ m/s in the considered time interval. This means that the melting front passes one step (one cell) along the Lagrangian grid over a time interval $\Delta t_{\rm m} = \Delta x^0/u_{\rm m} = 2.5$ ps. At this moment, the state of matter in the cell Δx^0 changes abruptly from the state of the solid phase to the state of the liquid phase.

Ones again, consider a cell that is adjacent to the melting front but not yet melted. It remains in a solid state 25 000 steps in time. There is very slow rise of temperature in a Lagrangian cell, while the melting temperature is strictly fixed value. Thus, 25 000 steps pass and suddenly, in one

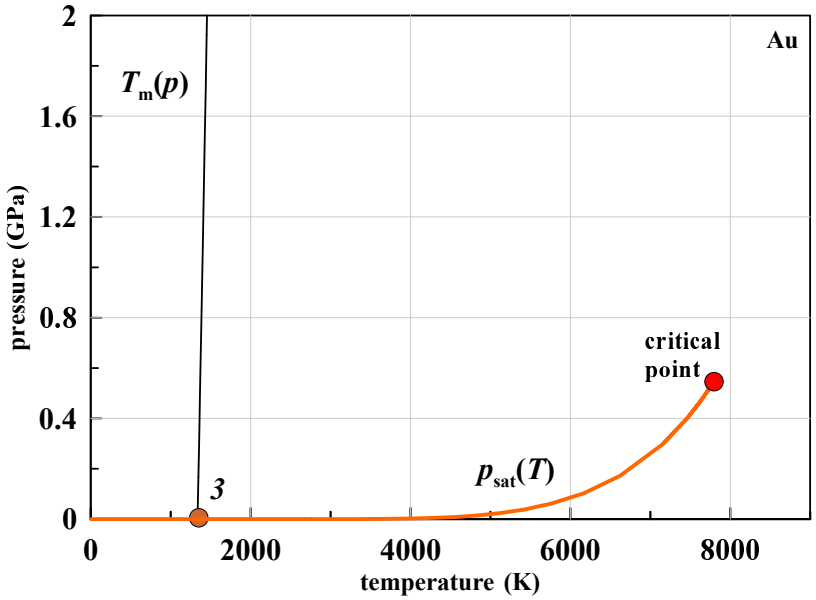

Figure 11. Melting curve $T_m(p)$ or $p_m(T)$ and the dependence of the saturated vapor pressure on the temperature $p_{\rm sat}(T)$. The data are taken according to the equation of state developed in the [55–60]. Marker *3* marks a triple point. The dependence $p_{sat}(T)$ ends at the critical point with the parameters 7800 K, 5300 bar and 5.3 g/cm^3. The vapor pressure at the triple point is negligible $p_{\rm sat}|_{(T=1337\ {\rm K})} = 4.3 \times 10^{-8}$ bar; the concentration of gold atoms in a vapor at the triple point is very low 2.3×10^{11} cm^{-3}. The boiling point is $p_{\rm sat}|_{(T=3243\ {\rm K})} = 1$ bar.

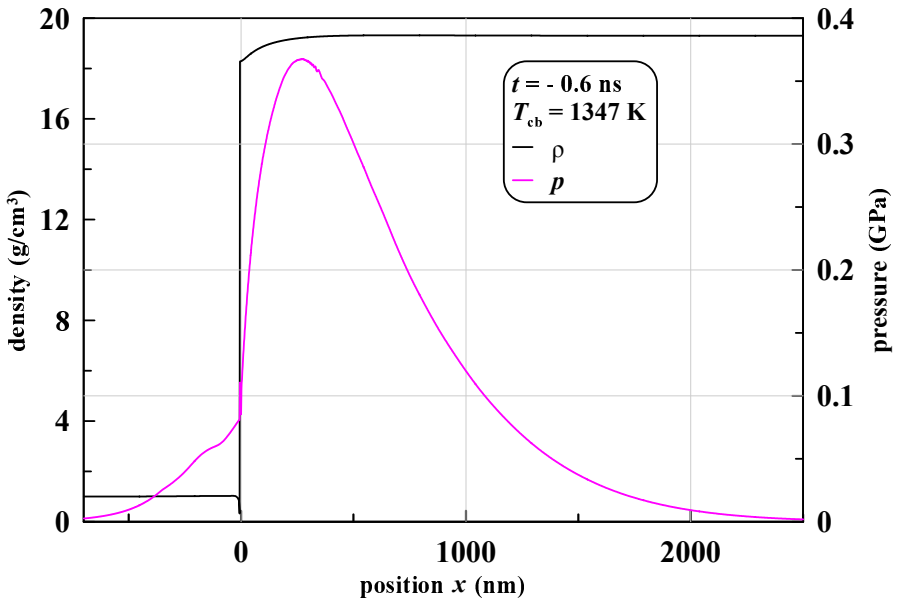

Figure 12. The density and pressure profiles at the same time as shown in figure 9. Acoustic perturbations (simple Riemann waves running into the water and into gold) composing together the pressure wave form smooth pressure profile. Tooth in figure 9 on the scale of x, adopted in this figure, is a very narrow splash at $x \approx 0$.

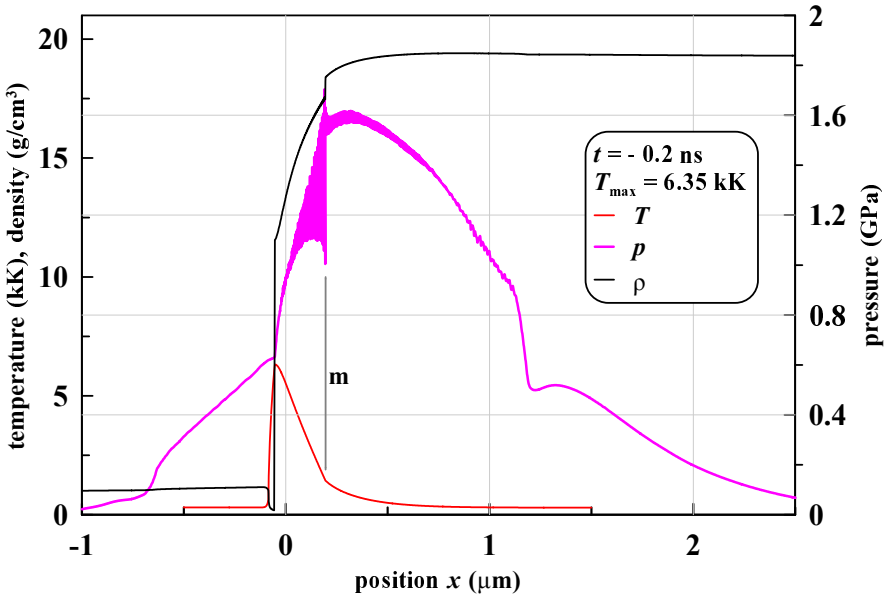

Figure 13. The middle of stage II (melting stage) is illustrated. The melting front is marked by the vertical line m. The strong heating of gold with a laser continues, the contact temperature is 6.35 kK, the melt thickness is a quarter of a micron. Because of the heating, the pressure increases with time and the pressure profile looks like a mound with a maximum shifted to the right of the heating layer, compare with figure 7. This shift is a consequence of melting. Two steep sections with high pressure gradients are clearly visible on the pressure profile. They are at $x = -0.6$ μm and $x = 1.2$ μm. Outside relative to the interval between these two sections, the p profile smoothly falls down to zero pressure. These outer portions of the pressure profile are acoustic waves emitted from the heating layer in stage I (namely before melting). Tilting of simple Riemann waves on steep sections due to the focusing characteristics leads to the origin of shock waves on these sections. Focusing is due to non-linear effects in simple waves. Rollover occurs later in time with respect to the moment of time $t = -0.2$ ns, shown in this figure. A sharp break in the pressure gradient at the contact boundary is due to the difference in the densities of the contacting substances.

step in time, the substance changes its state of aggregation from solid to liquid. This transition creates a pressure oscillation due to the density difference in the solid and liquid phases; as the Lagrangian cell expands, passing into the liquid. Further, this oscillation is carried by the characteristics departing from the melting front to the right and to the left. The spatial length of the oscillation is $\Delta t_{\mathrm{m}}\, c_{\mathrm{s}} \approx 5$ nm at the speed of sound in gold at a melting temperature of about 2 km/s.

We note that, in the case of a relatively long (subsonic) laser pulse under consideration with $\tau_{\mathrm{L}} = 0.5$ ns, the melting front is just the front. Its thickness is equal to the width of a single Lagrangian cell Δx^0. If we reduce the pitch Δx^0, then the oscillation length will be proportionally reduced; of course, the step can be greatly reduced so that the melting front is blurred into a transition zone with varying phase composition. The sharpness of the transition between the phases means that the melting process is described quite well in the approximation of the Stefan problem. In this sense, the subsonic laser pulse is qualitatively different from the "supersonic" pulse. The latter corresponds to the ultrashort pulse. The impulse becomes supersonic when $\tau_{\mathrm{L}} < d_{\mathrm{T}}/c_{\mathrm{s}}$. In the opposite case, the pulse was named above slow or subsonic. In the supersonic case, there is a transition zone of many Lagrangian cells of mixed composition, in which the

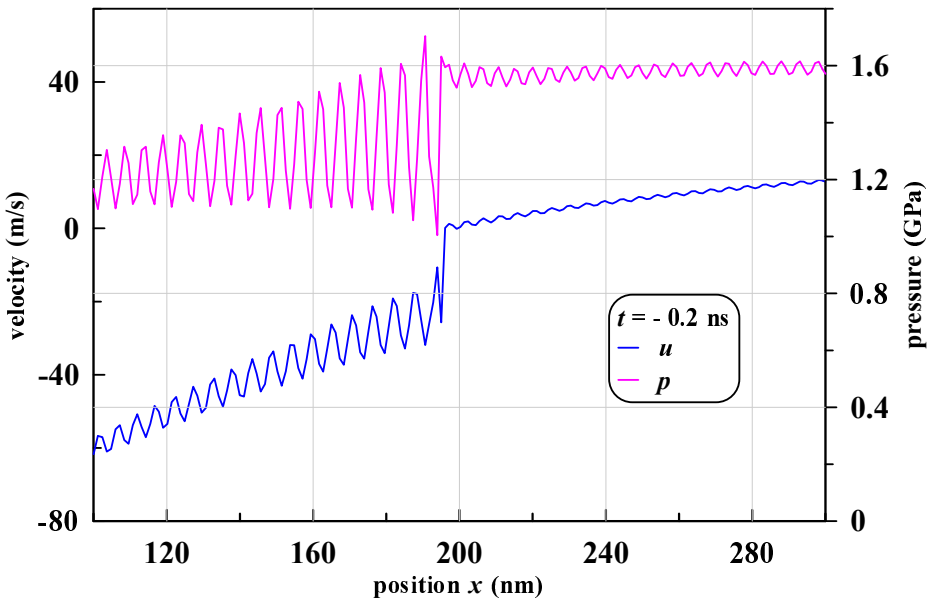

Figure 14. The jump associated with the melting front separates the liquid phase on the left and the solid phase on the right. The relation between the jump amplitudes and the Rayleigh line is discussed in the text. The movement of the melting front is subsonic, the Mach number is about 0.17.

solid and liquid phases coexist [61–63]; therefore, in the case of ultrashort exposure, there are no such pronounced oscillations as in figure 13. The composition gradually changes from pure solid to pure liquid at the edges of the transition zone.

The presence of oscillations is associated with the numerical-difference character of the used approximation. As one moves away from the melting front, the oscillation amplitude decreases. The first oscillation, which was formed at the time of the beginning of melting (shown in figures 9, 10 and 12), remains pronounced at subsequent points in time, see, for example, figure 13. In figure 13 steep sections on the pressure profile correspond to this oscillation. There are two such sites. At the moment of $t = -0.2$ ps, one of them is in water at $x \approx -0.6$ μm, while the second is in gold at $x \approx 1.2$ μm, see figure 13. The speed of sound in gold is greater, so the steep section in gold is located farther from the contact. The subsequent several oscillations, which were emitted by the melting front after the first, have already attenuated substantially. Their amplitude is small compared with recently emitted oscillations.

Because of the expansion of the metal during melting, a velocity jump occurs at the melting front. The amplitude of the jump is approximately $\Delta u_\mathrm{m} \approx 20$ m/s. With the acceleration of the substance at the intersection of the melting front, the existence of a small pressure jump at the front is connected. Speed and pressure jumps are shown in figure 14. The pressure jump amplitude is $\Delta p_\mathrm{m} \approx 0.18$ GPa. The velocity of the melting front relative to the substance is about $u_\mathrm{m} \approx 400$ m/s. At the melting front, conservation laws are fulfilled. The Rayleigh line $\Delta p_\mathrm{m} = j \Delta u_\mathrm{m}$ follows from the conservation of mass and momentum; here $j = \rho u$, u is the velocity of matter relative to the front, namely u_m. The values of Δp_m, Δu_m and u_m from our calculation satisfy the relation that is called the Rayleigh line.

Figure 15 shows the portion of the temperature profile near the melting front. On the profile, points mark the division points into Lagrangian cells. The horizontal straight line 1426 K gives the melting point according to the melting curve $T_\mathrm{m}(p)$. This curve is shown in figures 10 and 11. The melting point of 1426 K is reached at a pressure of 1.5 GPa. The pressure value of 1.5 GPa in

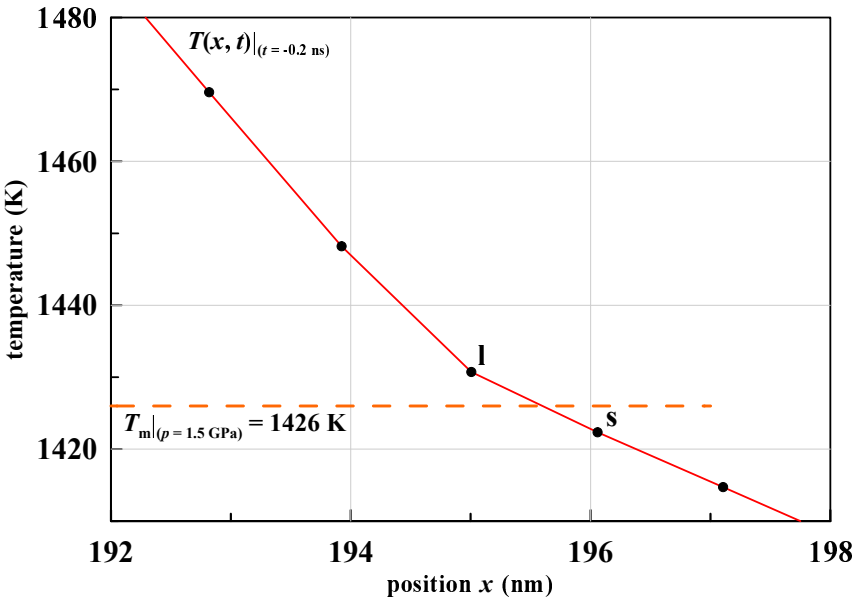

Figure 15. Temperature distribution over Lagrangian nodes and cells near the melting front at time $t = -0.2$ ns. Explanations regarding the jerks of state from solid to liquid and relative to the temperature gradient are given in the text. The state changes when the node s (solid phase) reaches a melting point of 1426 K. This is the melting point at a pressure of 1.5 GPa in the vicinity of the melting front, see figure 14.

the region of the melting front at the time $t = -0.2$ ns is taken from figure 14. The temperature difference between points s (solid phase) and l (liquid phase) in figure 15 is equal to 8 K. The temperature in the Lagrangian cell s grows at a rate of 0.03 K in one integration step over time. Over the order of 100 time steps, the temperature in the Lagrangian cell s will exceed the melting point of 1426 K. At the same time, the cell will change its status—it will turn from solid to liquid (melt). The formation of the next oscillation is due to such melting jerks.

The temperature gradient is higher in the liquid phase (see figures 13 and 15). Two factors determine this effect. First, melting occurs at this stage, that is new and new portions of solid gold are melted. In order to cover the costs associated with the latent melting heat Q, it is necessary that the heat flux q_{l} to the front exceed the heat flux q_{s} from the front: $q_{\text{l}} - q_{\text{s}} = Q\rho_{\text{s}}u_{\text{m}}$, where Q—the heat of fusion per unit mass. Secondly, the coefficient of thermal conductivity is about 2–2.5 times lower in the liquid phase; the thermal conductivity model used in the calculation takes into account the change in thermal conductivity during melting. Therefore, even at $Q = 0$, the temperature gradient will be higher in the liquid.

In the case of long pulses, the resulting pressure is small (compared with the bulk modulus of the metal). Therefore, the substance is located along the boiling curve in accordance with the temperature distribution in gold, figure 16; the boiling curve is called the right branch of the binodal (phase coexistence curve), that is the expansion of matter is mostly due to the heat. The available pressure has little effect on the density (in the sense of deviation from the boiling curve).

In figure 17 the hydrodynamic profile is compared with the boundaries of the phase transitions of the first kind on the plane ρ, p. We see that on the moment of time, shown in figure 17, all gold (points *1–2–3*) is still located to the right of the critical density of gold 5.3 g/cm^3. Additional heating is needed to exceed the critical temperature (see figure 16) and to lower the density below the critical value (see figure 17).

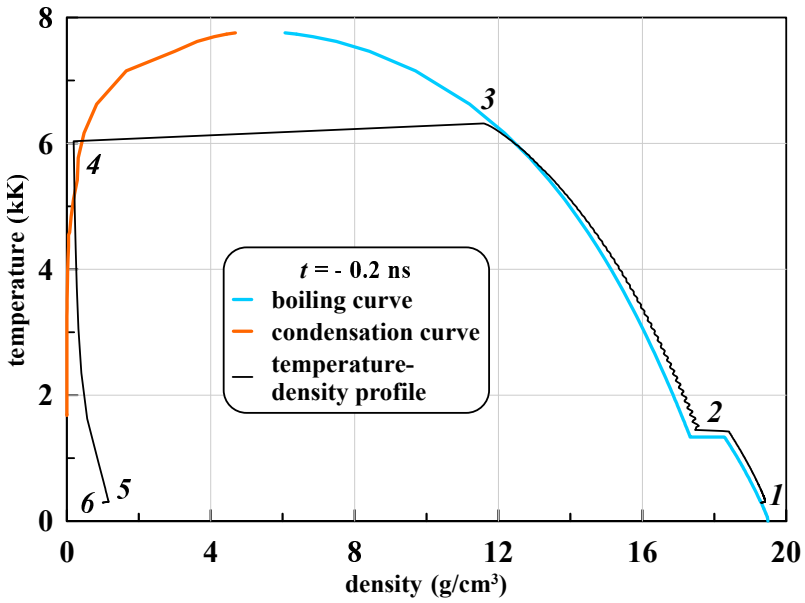

Figure 16. The state of matter in the phase diagram at time point of $t = -0.2$ ns. Together with the phase equilibrium curves, the density and temperature profiles are plotted here in parametric form: $\rho(x,t)|_{(t=-0.2\ \mathrm{ns})}, T(x,t)|_{(t=-0.2\ \mathrm{ns})}$. The parameter that runs through the profile is the coordinate x. Points designation: *1*—undisturbed gold deep in the target; *2*—melting front repeating the density jump at the triple point (see figures 13–15); *3*—maximum temperature on contact with water (see figure 13); *3–4*—density jump (temperature is continuous!) from gold to water at their contact boundary (see figure 13); *4*—hot water adjacent to the contact; *4–5*—temperature profile in water; *6*—water far from the contact. Of course, the states of water are irrelevant to the gold condensation curve. Under the influence of the pulse, the temperature of gold rises. Therefore, point 3 rises higher and higher along the boiling curve. However, there is no gold evaporation, since the pressure is higher than the saturated vapor pressure, see figure 11. Evaporation (appearance of dense non-ideal gaseous gold) will start when point *3* reaches the critical point. Real evaporated gold appears when pressure drops down below critical pressure. This problem is considered in the next section.

7. The excess of the critical temperature of gold, the appearance of a contact layer of gaseous gold

Over time, the temperature of the metal near the contact rises under the laser pulse action. As mentioned above, the flow in its development goes through several stages: stage I ends with the start of melting; stage II is completed with the achievement of the critical temperature of the metal. At stage III, three layers are adjacent to the metal contact with water. With the transition from stage II to stage III begins the formation of a layer of gold in the gaseous state. So at stage III, a layer of gaseous gold is located near the contact, then a layer of melt follows, and then there is a solid phase.

Figures 18–21 show the situation at time $t = 0$. Stage III begins: the contact temperature exceeds the critical temperature $T_{\mathrm{cr}} = 7.8$ kK, and the density falls below the critical value $\rho_{\mathrm{cr}} = 5.3$ g/cm^3. But the pressure is about 4 times the critical value of $p_{\mathrm{cr}} = 0.53$ GPa. As is known, the density range $\rho < \rho_{\mathrm{cr}}$ formally is related to the gas phase. At a density of $\rho > \rho_{\mathrm{cr}}$, the substance is assumed to be in the liquid phase. Of course, above the critical point such a division is conditional. A substance at $\rho \sim \rho_{\mathrm{cr}}$ is called a fluid or nonideal gas. We are talking about the gaseous state, not the gas state, in the case of nonideal gas. Although in the case

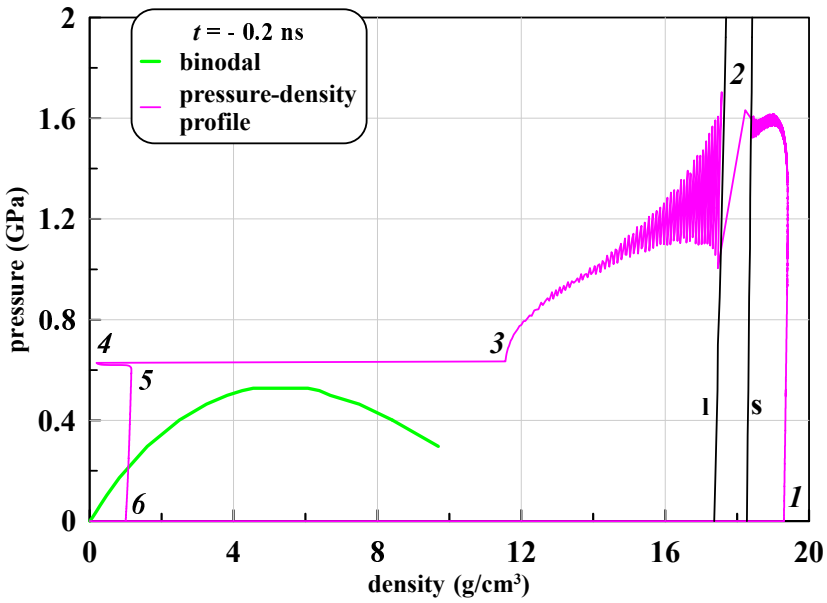

Figure 17. The hydrodynamic profile is built together with the phase equilibrium curves upon the ρ–p plane of Au. Numbers *1–6* indicate the same states as in the previous figure 16. We see that the pressure at the hottest point of gold is still above the critical pressure of gold. The hottest is point *3*. It is on contact with water. The letters s (solidus) and l (liquidus) indicate melting curves bordering the corridor of the existence of a mixture of solid and liquid phases. The intersection of this corridor with the instantaneous profile of the density and pressure distributions corresponds to segment *2* in figure 16. The pressure at the intersection of the melting front abruptly decreases, compare with figures 13 and 14. This is caused by spatial expansion of liquid relative to solid crossing the melting front.

shown in figures 18–21, the gold pressure in the gas layer between the boundaries *2* and *3* in figure 19 is close to the pressure given by the formula for the ideal gas $p = nk_{\mathrm{B}}T$ for the density and temperature in this layer. Note that according to used in the calculation of the equation of state of gold [55–60], compressibility factor of $p/(nk_{\mathrm{B}}T)$ is equal to 0.3 at the critical point.

By the time point $t = 0$ gold absorbed half the energy F_{abs} of the pulse. From figures 18–21 it follows that the gas layer of gold *2–3* (see figure 19) is formed at the moment $t \approx 0$. The coincidence with the maximum of the pulse $\tau_{\mathrm{L}} = 0.5$ ns, $F_{\mathrm{abs}} = 900$ J/cm^2 occasional. Indeed, if the energy of F_{abs} were greater, then the achievement of the gas state would occur before the maximum pulse $I \propto \exp(-t^2/\tau_{\mathrm{L}}^2)$.

In figure 20 layers are shown: *1–2* hot water, coordinates $x = -167$ and -125 nm, thickness 42 nm; a layer of gas gold *2–3* with coordinates -125 and -113 nm, thickness 12 nm and a layer of melt almost 400 nm thick. The melting front coordinate at time $t = 0$ is 278 nm. The coordinates of x are measured from the initial position of the contact boundary.

We emphasize that in the gas state layer *2–3* in figure 19 falls around the critical point from above. That is, layer *2–3* is not formed as a result of evaporation of the heated condensed matter. Pressure in region *1–2–3* in figure 19 above the saturated vapor pressure $p_{\mathrm{sat}}(T)$. This pressure is above the maximum value that the function $p_{\mathrm{sat}}(T)$ can have, that is. above the critical pressure p_{cr}, see figures 11 and 21. Layer *2–3* in figure 19 is formed as a result of continuous temperature growth on the temperature profile $T(x,t)$ of gold over time t during the action of the laser pulse: $T(x^0,t_2) > T(x^0,t_1)$, if $t_2 > t_1$, here x^0—Lagrangian coordinate On the phase plane ρ, T this profile is located along the melting curve, see figures 16 and 20. To the

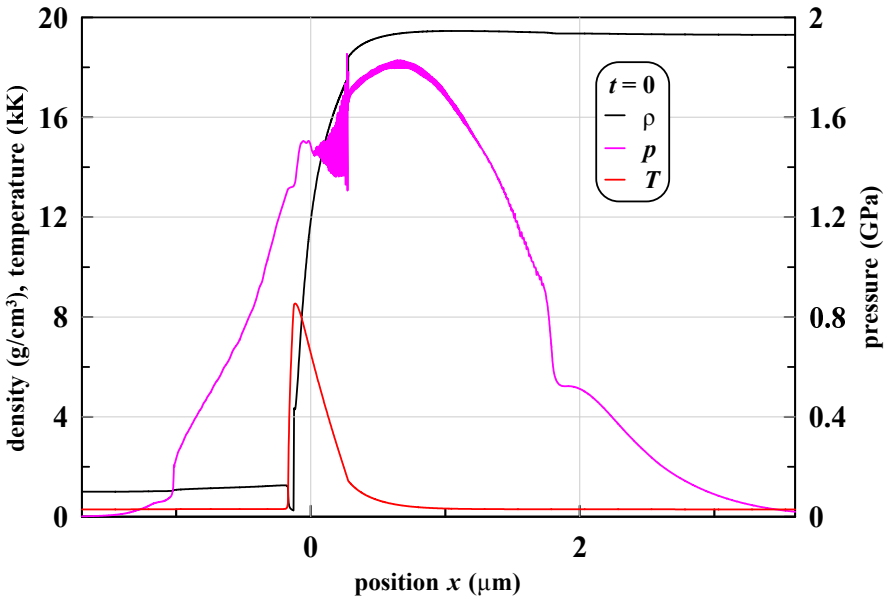

Figure 18. Profiles of density, temperature and pressure at the time instant $t = 0$. The pressure profile contains information about changes in the intensity of the laser pulse over time. The moment $t = 0$ is close to the moments of overturning of simple waves in water and gold: the steep sections on the pressure profile are close to the vertical segments at the points of inflection. By the time $t = 0$, gold absorbed half the energy $F_{\text{abs}}/2$ of the incident pulse $I(t) = I_0 \exp(-t^2/\tau_{\text{L}}^2)$. In the calculation described in this paper, we have: $\tau_{\text{L}} = 0.5$ ns, $F_{\text{abs}} = 900$ mJ/cm^2. At $t > 0$, the intensity of $I(t)$ decreases as compared with the maximum value of I_0.

instantaneous profiles $T(x,t)$, $\rho(x,t)$ there correspond points *1* (state far in volume), *2* (melting front) and *3* (contact) in figures 16 and 20.

Due to the increase in temperature at the contact, the top point *3* of the profiles $T(x,t), \rho(x,t)$ moves up along the melting curve, compare with figures 20 and 16. Point *3* in figures 20 and 16 reaches the critical value $T_{\text{cr}} = 7.8$ kK and then (with continued heating) it begins to exceed this value if the energy input F_{abs} is large enough. The temperature profile $T(\rho;t)$ in figure 20 goes slightly above the boiling curve, because the pressure is higher than $p_{\text{sat}}(T)$.

Let the saturated vapor above the liquid phase form as a result of the evaporation of this liquid. Then there are two states on the phase plane ρ, T: one on the boiling curve and the other on the condensation curve. The pressure in the vapor–liquid system is equal to the saturated vapor pressure $p_{\text{sat}}(T)$, see figure 11. In our situation, as it is said, evaporative formation of a layer of pure gold vapor (without water) is impossible until the condition $p > p_{\text{sat}}(T)$ is satisfied.

Compare the number of gold atoms that have passed the gas–vapor phase by evaporation (path B) and by heating above the critical temperature point $T_{\text{cr}} = 7.8$ kK by ΔT of the order of one or several thousand degrees (path A). The evaporation of gold atoms into water takes place even in the profile situation shown in figure 16. The corresponding number of evaporated atoms N_B is small compared to the number of atoms N_A in interlayer *2–3* in figure 19. In our code with the Lagrangian coordinate x^0 there are no mixed cells in which both gold atoms and water molecules would be present. Therefore, the processes of evaporation into water and mutual diffusion are not taken into account. A molecular dynamics approach [54] is required to analyze these processes.

As mentioned, figures 18–21 show the situation at the time $t = 0$ of the laser pulse maximum. Then the intensity absorbed in the metal begins to decrease with time. However, the growth of

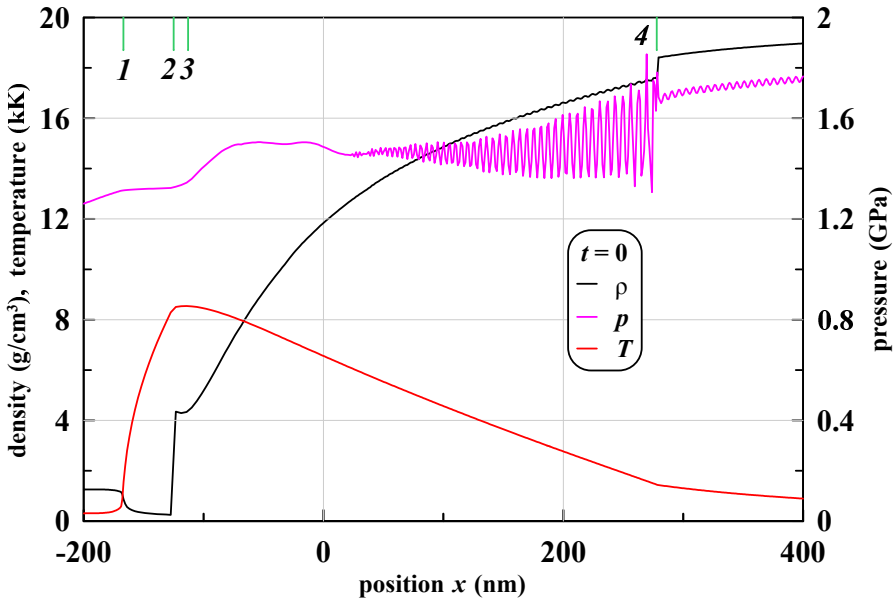

Figure 19. The structure of the contact zone at $t = 0$ is shown. Strips *1, 2, 3* and *4* mark the boundaries of the layers. To the left of *1* is cold dense water, the thermal conductivity of water is calculated from the data taken from the literature. Between the boundaries *1* and *2* there is a layer of hot partially dissociated water, *2*—gold–water contact. The equation of state of water is taken from [70]. Layer *2–3* is gaseous gold. Layer *3–4* occupies the liquid phase, *4*—the melting front, it moves relative to the substance to the right. To the right of *4* is the solid phase.

the temperature and pressure maxima $T_{\max}(t)$, $p_{\max}(t)$ continues for some time, that is, these maxima are shifted in time relative to the intensity maximum $I(t)$. Stage IV starts when the formation of a dip in the pressure profile begins. The following section is devoted to this topic.

8. Emission of acoustic disturbances from the heating layer

8.1. Weak disturbances

Acoustic disturbances track heating history $I(t) : I(t) \to T(x,t)|_{(x\sim 0)} \to p(x,t)|_{(x\sim 0)} \to p(x \pm ct)$, where $x \sim 0$ is the hot metal layer *5* in figure 7 (area of heating), the letter c with the plus sign is the wave going into the water. At that time, c is the speed of sound in water. Similarly, c minus refers to the wave propagating in gold. Figure 22 shows the development of the acoustic field at the final stages of laser action, when the intensity $I(t)$ decreases.

The increase in the maximum temperature of $T_{\max}(t)$ (maximum over the instantaneous temperature profile) continues at $t > 0$, despite the decrease in the intensity of $I(t)$. Indeed, energy is still being supplied to the system. A slow decrease in the value of $T_{\max}(t)$ begins at $t \approx 0.4$ ns when the thermal conductivity losses into bulk gold begin to exceed the laser heating power. The highest temperature in space and time $T_{\max-xt}$ is 11.3 kK for the considered laser pulse. Radiation losses $\sigma_{\text{SB}}T^4 \sim 10^9$ W/m^2 in the considered range of times and temperatures are small in comparison with the electron heat flux in metal $\kappa \mathrm{d}T/\mathrm{d}x \sim 10^{12}$ W/m^2 at $\kappa \sim 100$ W/m/K, $\mathrm{d}T \simeq 8$ kK, $\mathrm{d}x \simeq 300$ nm.

At $t \approx 0.3$ ns the formation of a dip on the pressure profile $p(x,t)$ in the zone of the heating layer (the zone near the contact boundary) begins. This is shown in figure 22. The temperature rise in the heating region $\mathrm{d}T/\mathrm{d}t$ first slows down and then stops. After that decrease of temperature begins. The beginning of stage IV is connected with the formation of a dip in

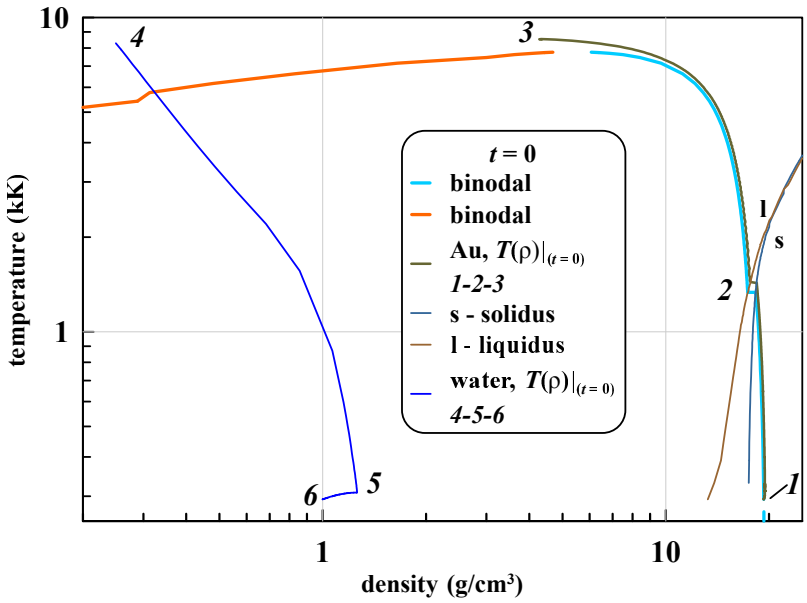

Figure 20. Temperature profile $T(\rho,t)|_{(t=0)}$ on the phase plane ρ–T. The gradual heating by the laser leads to the fact that the temperature on the profile $T(\rho,t)|_{(t=0)}$ rises above the critical value $T_{\rm cr} = 7.8$ kK. The single (for water and Au) profile $T(\rho,t)|_{(t=0)}$ is divided into two *1–2–3* (Au) and *4–5–6* (water) pieces. A density jump of *3–4* refers to the contact boundary, compare from figure 16, where a single profile is shown. Au and water densities at the contact are 4.35 and 0.25 g/cm^3. A single density profile shows a profile where gold and water are not separated. Here they are separated. Curves s (solidus) and l (liquidus) are continued through the triple point to the metastable area [55–60]. Point 1 corresponds to gold at a great distance from the contact, where the temperature is equal to room temperature 300 K.

the p profile. Gradually, a single pressure bump splits into two different waves propagating into gold and water, see figure 22.

The profile of the emitted waves is determined by the current pressure in the contact zone. Waves are emitted from the contact zone. There is a substance with high entropy in the contact zone. The expansion of a highly entropic substance compresses mechanically the surrounding water layers to the left and gold to the right of the contact zone. These are passive layers with low entropy. Compression is carried out by acoustic waves radiating by an active substance with high entropy.

The derivation of formulas (7)–(9) in section 5 was based on two relations. Firstly, this is the relationship between velocity and pressure in a simple Riemann wave $p = z_{\rm w} u$ and, secondly, this is the energy conservation law $p\,{\rm d}V = I\,{\rm d}t\,S$, $p\,u = I$, hence $p^2 = I$; the relation is written up to factors. After the end of the laser pulse, the second ratio becomes unnecessary.

But the first relation remains. It turns out that the expansion continues even after the termination of the laser exposure. If the active substance has a pressure $p > 0$, then there will be an expansion rate $u > 0$ of this substance. Thus, the emission of acoustic waves from the active layer continues after the laser is turned off.

The pressure gradually decreases as the active layer expands. Thus the expansion of the active layer after turning off the laser is responsible for the formation of the tail of the acoustic waves propagating in water and gold.

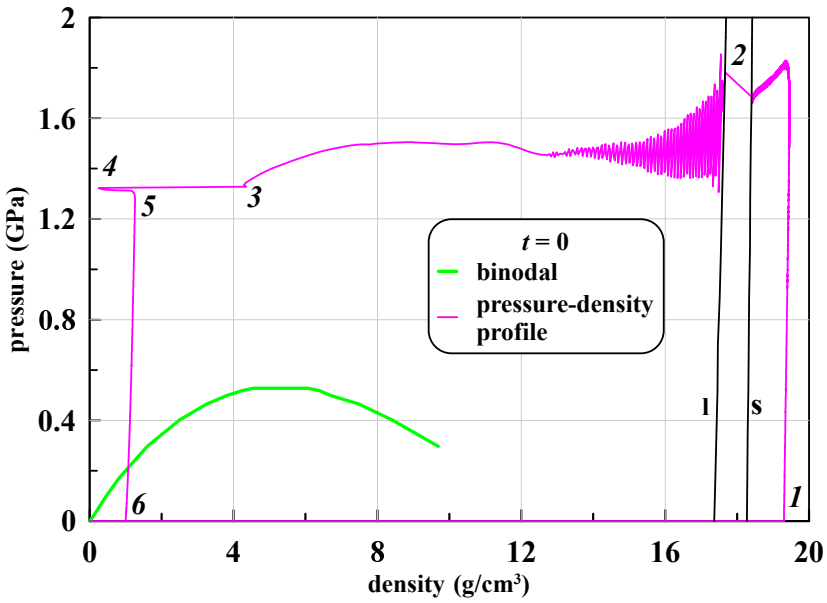

Figure 21. Pressure profile $p(\rho, t)|_{(t=0)}$ on the phase plane ρ–p is shown. For the time elapsed from the previous time point $t = -0.2$ ns, see figure 17, the pressure has increased significantly: twice times near contact and 7% in its maximum value. The maximum pressure is in the solid phase behind the melting front—we have to average over oscillations in liquid. The meaning of numbers *1–6* is the same as in figures 16, 17 and 20. Note that the corresponding to gold *1–2–3* profile, which was just above the boiling curve in figure 20 and 16, here it is far removed from the boiling curve. This is due to the low compressibility of the condensed phase. Surprisingly, this is also true for states that are to the left of a critical point on the density axis.

8.2. Shocks

A shock wave is formed from a steep section in water in figure 22; the existence of two steep sections was discussed in figures 13 and 18. Appearance of these two steep sections is consequence of the transition from stage I (all gold is solid) to stage II (dynamics with a molten layer). The volumetric water module of 2.25 GPa is almost two orders of magnitude lower than the gold module of 180 GPa. Therefore, the tilting of a steep section in water occurs much earlier than in gold. Although the water pressure is slightly lower than pressure in gold, see figure 22.

As was said, the heating history of $I(t)$ is written in the $p(x \pm ct)$ profile of the Riemann simple wave. In the shock wave, this history gradually disappears, because flow behind the shock is subsonic, thus the particular portions of the Riemann wave come to the shock and disappear in the shock. Gradually, the wave transforms into a triangular shock wave, compare the profiles at time points of 0.3 and 0.4 ns with the profile at time of 1 ns in figure 22.

The amplitude and evolution of the shock wave in the metal are important for laser peening. For peening, it is necessary that (i) namely a shock wave be formed in the metal (smooth compression wave weakly plastically transforms solid) and (ii) that the amplitude of this wave be above the Hugoniot Elastic Limit. Plastic deformations remaining behind the front of a plastic shock wave are responsible for the hardening of the surface layer of the target with respect to fatigue failure and corrosion. This is the main purposes of the peening.

In our approach, we examined the formation and propagation of a shock wave in a metal target. Two important aspects of laser shock wave initiation were analyzed. Firstly, this is a joint analysis of the wave in the metal and the flow in the surrounding water. Secondly, the accompanying processes of melting and evaporation in the heated surface layer of the target

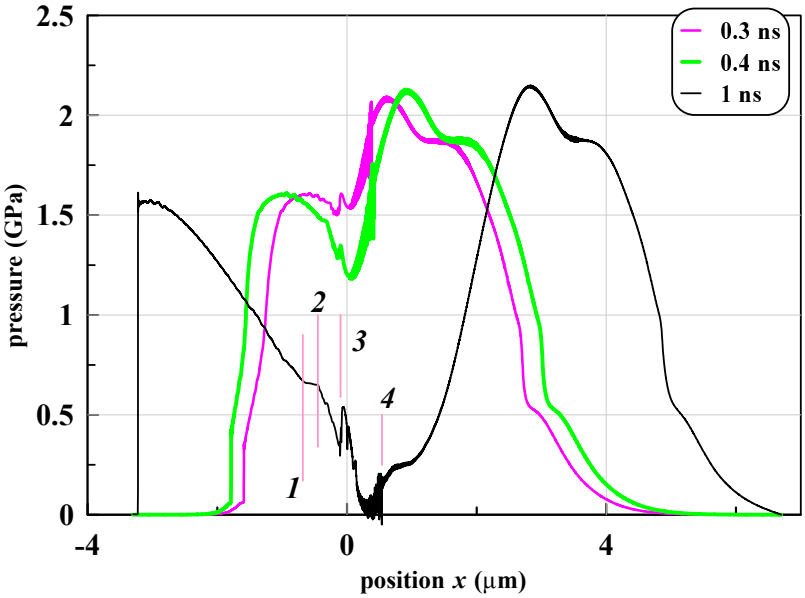

Figure 22. Evolution of the pressure field after the start of a decrease of the absorbed laser pulse intensity $I(t) \propto \exp(-t^2/\tau_{\rm L}^2)$, $t > 0$. Recall that $\tau_{\rm L} = 0.5$ ns. At times about $t = 0.3$ ns, the formation of a dip in the pressure profile begins due to a decrease in the rate of heating of the substance. At $t \approx 1$ ns there is a complete separation of waves running to the left (into the water) and to the right (into gold). Points *1, 2, 3* and *4* mark the boundaries of the layers. As in figure 19, these are the boundaries of the hot water layer *1–2*, the gaseous gold layer *2–3* and the melt layer *3–4* at the time $t = 1$ ns.

were studied. But in our approach to nanosecond laser shock peening (ns LSP), the plastic EOS of gold was used. Therefore, the elastic-plastic phenomena were not reflected. Previously, the problem of plastic transformations was solved for the case of ultrashort pulse: see work with molecular dynamics [7–9, 11], as well as hydrodynamic studies in which the phase transitions were embedded together with elasto-plasticity [64, 71, 72].

There are two LSP technologies: the traditional ns LSP with confinement of metal expansion by water and modern femtosecond (fs) LSP. Peculiarities of the fs LSP were discussed above in sections 2 and 3. These peculiarities are caused by increase of the Hugoniot elastic limit (HEL) in ultrashort shock waves. So, plastic peening is absent even behind sufficiently powerful ultrashort shocks.

9. Evaporation, diffusion, condensation

We discussed above the active layer (a layer of high entropy) in connection with its role in the mechanics of sound emission. Now let us look at another role of the active layer. The fate of the active layer is important for the subsequent later stages in the case of laser ablation into a liquid (LAL, technology for the production of suspensions of nanoparticles). In several nanoseconds, the process of intense diffusion of gaseous gold into hot water ends—intense diffusion continues until the contact temperature is above the critical temperature and the surface tension separating liquid gold and hot water is absent [73]. Starting from several nanoseconds to about a dozen to hundreds of nanoseconds, gold vapor is condensed into clusters and nanoparticles [51]. All this (diffusion and condensation) takes place in the substance of the active layer.

Condensation is illustrated in [51, figures 21 and 22]. The calculations of condensation in this paper were performed using the molecular dynamics (MD) method. In our MD simulations,

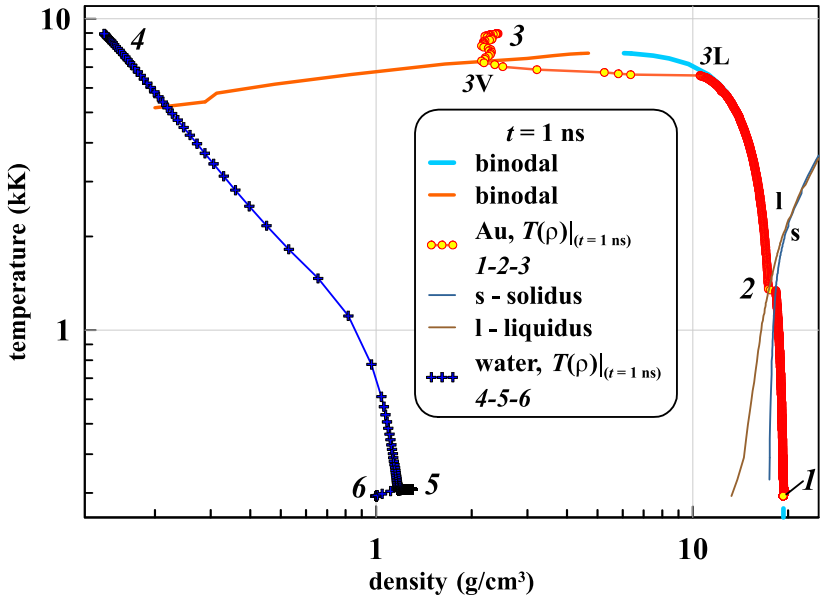

Figure 23. Profile presented in previous figure 22 is shown here at the ρ–T phase diagram. The blue binodal is a boiling curve. The orange binodal is a condensation curve. They come from left and right sides to the critical point. There is a density jump *3*–*4* from gold to hot rarefied water. Part of the profile *1*–*2*–*3* relates to gold. Point *1* presents the layers of gold before the shock in gold. Point *2* marks a melting front. As a result of cooling after finishing of a laser pulse the temperature drops below critical temperature. The point *3*L is the most hot liquid (L) gold with entropy below critical entropy $s_{\rm cr}$. The curve *3*–*3*V (V—vapor) corresponds to gaseous gold with entropies higher than $s_{\rm cr}$. The points *4*–*5*–*6* present water. The profile *4*–*5* consists from two pieces. One corresponds to hot rarefied high entropy layer of water, while other is a piece of profile behind shock wave in water.

spatial expansion of the substance is taken into account (this is important feature 1). The calculations were carried out for a gaseous dense pure gold and for a mixture of gold vapors with water in a one to one ratio. This ratio corresponds to the central region of the water-gold mixture in the active layer. In our MD simulations we are interested in analyzing the condensation process at temperatures comparable to the critical temperature (important feature 2).

Earlier in the literature, condensation modeling was performed for much lower temperatures (less than half of the critical temperature) and, without taking into accounts the spatial expansion of the vapor (the important features 2 and 1 emphasized above). Let us refer to this approach as a classical approach. But this particular approach is not interesting for the problem of ablation in a liquid. The latest information on the classical direction of researchs is contained in the articles [74, 75].

In work [74] the region of the phase diagram in the form of a strip above the left branch of the binodal (the curve of vapor-liquid equilibrium) was studied; the left branch is called the condensation curve, the right branch is called the boiling curve. It was shown in paper [74] that the decrease in the compressibility factor compared to unity is not due to the attraction of closely spaced monomers (the concentration of monomers is quite high); the compressibility factor characterizes the degree of deviation from the behavior of an ideal gas. The indicated decrease in the compressibility factor occurs due to the condensation of part of the monomers into clusters (dimers, trimers, etc.). The formation of the condensation component takes place above (!) the condensation curve, which, by definition, separates the gas and the two-phase

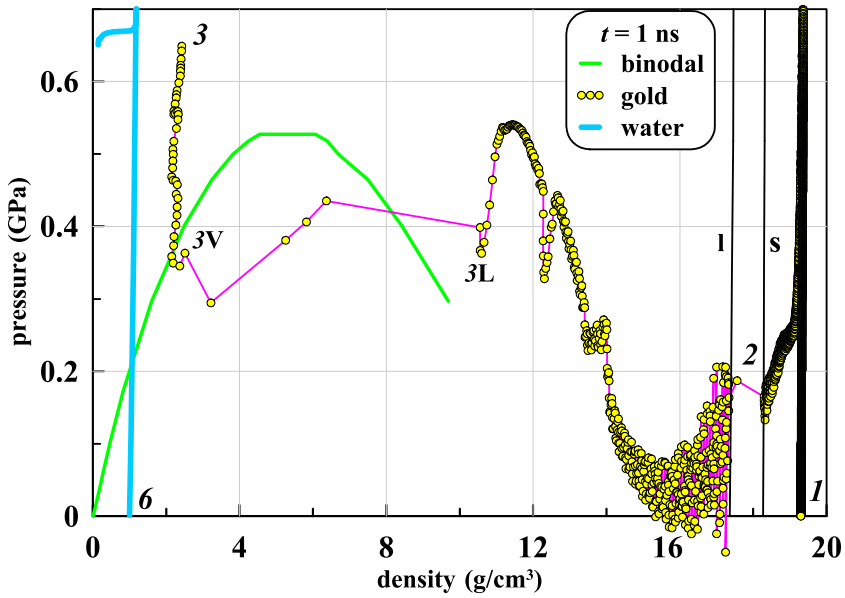

Figure 24. The plane ρ–p is important for the interpretation of mechanical phenomena. The compression wave in gold (see figure 22) is cut off here to increase the vertical scale. We clearly see appearance of gaseous gold *3*–*3*V with $s > s_{\mathrm{cr}}$. This layer of gold will condensed later into nanoparticles during expansion and cooling. Addition to nanoparticles from evaporation of the liquid gold *3*L–*2* is small.

mixture. Non-ideal gas is usually thought of as an ensemble of monomers located at fairly close distances. Clusters are virtual. Their virtuality means that clusters are permanently formed due to condensation and also are constantly destroyed due to evaporation. It turns out that the liquid phase nuclei are present above the binodal. Moreover, in the vicinity of the critical point, their presence is dynamically significant—the compressibility factor decreases several times in comparison with unity. The presence of a cluster component leads to conclusions about the need to revise theory of kinetics of condensation of supercooled gas below the binodal.

Let us return to our non-classical condensation (important features 1 and 2) corresponding to LAL. In later times (tens of microseconds), our active layer with condensation products inside fills a bubble of a mixture of high entropy water and condensate of nanoparticles [73]. The foregoing relates specifically to the nanosecond action, when there is no thermomechanical formation and destruction of the foam of the molten metal, as in a femtosecond action. Mechanical destruction of foam on a capillary scale is another channel for the formation of the size distribution of a droplet cloud.

10. Critical entropy

In figures 23 and 24, the profile shown in figure 22 is projected to the phase planes. The profile in figure 22 refers to a time moment of 1 ns. The profile describes the instant situation in gold and in water.

By comparing pairs of figures 16 and 17, then 20 and 21 and then pair of figures 23 and 24, we see the following. As heating, the profile in the phase diagram rises up (the first two pairs of diagrams), the pressure begins to exceed the critical pressure (first two pairs of diagrams). Then a pulse finishes, the pressure decreases, and the profile drops down. At some point in time, the pressure p in the active layer becomes lower than the pressure p_{cr}, which refers to the critical point. The pair of figures 23 and 24 corresponds to this situation.

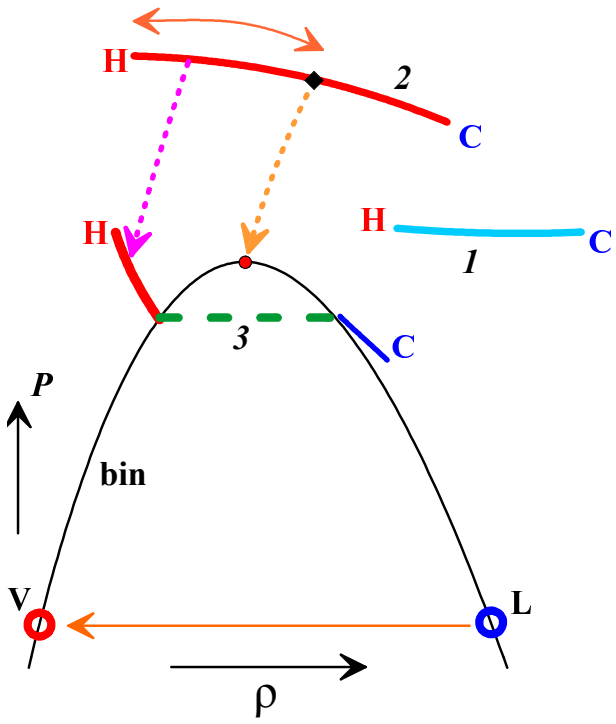

Figure 25. The usual evaporation L–V is contrasted here with the appearance of gaseous gold in our case with nanosecond laser exposure with fluence near the threshold of optical breakdown of water. In our case gaseous is gold with high entropy $s > s_{\rm cr}$. The piece of the profile *2* from the point H to the black rhombus corresponds to gold with entropy $s > s_{\rm cr}$. Hot gold expands and therefore evolves in direction to smaller density: the evolving profiles *1–2–3* follow each other. The end points C and H of the intervals *1*, *2*, *3* correspond to hot (H) and cold (C) gold.

To clarify this, figure 25 has been added. In figure 25, the signs L (liquid) and V (vapor) and the arrow connecting them correspond to usual evaporation. This arrow indicates the direction of evaporation. In this case, the temperature of the liquid L is kept constant that is energy consumption for evaporation is compensated by heating the liquid. There is an outflow of the evaporated substance from the evaporation surface (therefore we plot the arrow). This flow is either without collisions (Knudsen regime, the Hertz-Knudsen formula, evaporation into a vacuum), or a diffusion flow. With diffusion outflow, the evaporation rate is, of course, much lower than in the Knudsen regime.

In the case of our long laser pulse, the situation is different (see figure 25). Namely, there is a time interval in which a near-surface layer of hot gold is created with entropy values s higher than the entropy value $s_{\rm cr}$ corresponding to a critical point.

Let us consider the evolution of the active zone; this is the layer near the contact. A change of profiles *1–2–3* in figure 25 presents the evolution. Profile *1* refers to the situation shown in figures 13, 19, and 17. Profile *2* represents the instant shown in figures 19, 20, and 21. Finally, profile *3* in figure 25 refers to the situation in figures 22–24. There is the time interval around the time instant corresponding to profile *2* when a surface layer of gold is created with supercritical entropy values $s > s_{\rm cr}$. At sufficiently high values of absorbed energy $F_{\rm abs}$, mainly a substance with high entropy $s > s_{\rm cr}$ creates a condensate of gold nanoparticles during unloading. Let the mass of a substance with high entropy $s > s_{\rm cr}$ be $m_{\rm s-cr}$. Additions to this condensate associated with evaporation through the gold–water contact boundary at contact temperatures $T < T_{\rm cr}$, differently depend on the absorbed energy $F_{\rm abs}$. Surface tension of liquid gold is finite if $T < T_{\rm cr}$.

Let the mass of additions be $m_{\rm cold}$. The mass $m_{\rm cold}$ exponentially increases with increasing $F_{\rm abs}$. This is connected with exponential temperature dependence of saturated vapor pressure. The increase in mass $m_{\rm cold}$ with increasing energy $F_{\rm abs}$ continues until a layer of supercritical gold $s > s_{\rm cr}$ appears. In this case, the increase in mass is $m_{\rm cold}$ with increasing energy is saturated. Let us say that the corresponding value of $F_{\rm abs}$ is threshold.

Conversely, the mass $m_{\rm s-cr}$ monotonically increases with increasing energy $F_{\rm abs}$ above the threshold.

As stated above, there are two contributions to the condensate (the condensate is a source of nanoparticles in ns LAL, laser ablation in liquid). The first of them is associated with evaporation through the capillary boundary and with the diffusion of gold vapor in water. The second contribution is gained when the contact temperature rises above the critical temperature $T_{\rm cr}$. Then the capillary boundary disappears, and with it the need for evaporation also disappears. Mutual diffusion of gold and water takes place. With equal lengths of time allocated to create a diffusion layer, the mass of the second contribution is greater.

The fact is that the capillary boundary serves as a powerful barrier to evaporation. Due to the barrier, saturated vapor pressure decreases exponentially with decreasing temperature.

There are two time intervals ("a" and "c") on which the first mechanism for accumulation of the diffusion layer works. Between them is the time interval ("b"), on which the second contribution operates. These three intervals correspond to three profiles in figure 25. In the intervals "a" and "c", the temperature in condensed gold is below the critical temperature $T_{\rm cr}$. While in the interval "b" temperature is above $T_{\rm cr}$.

In the interval "a" evaporation proceeds through the capillary barrier from the point H at the profile *1* in figure 25. This barrier separates two immiscible media. In the interval "b" the capillary barrier is absent. Direct diffusion between two miscible substances works. In the interval "c" evaporation through the capillary boundary comes from the point where the cold part of the profile *3* intersects the boiling curve in figure 25.

As one can see in the case of profile *1* in figure 25, the contact boundary (through which the vaporization of gold into water occurs) is not on the binodal of pure gold. The fact is that we are dealing with a binary system of gold and water. Let the pressure in bynary system significantly exceed the critical pressure which in the case of pure gold is 5300 bar. Then the binodal will undergo significant changes in the vicinity of the critical point and at the condensation curve. Temperature dependence of saturated gold vapor pressure $p_{\rm sat}(T) \to p_{\rm sat}(T, p_{\rm sum})$ and the dependence of the surface tension coefficient on temperature $\sigma(T) \to \sigma(T, p_{\rm sum})$ will also be changed. Here $p_{\rm sum}$ is the pressure in the binary system. In the region of the diffusion mixture, the total pressure is the sum of the partial pressures of water and gold vapor. Gold vapor pressure is limited by the critical pressure for pure gold $p_{\rm cr}$.

There is currently no information on the functions $p_{\rm sat}(T, p_{\rm sum})$ and $\sigma(T, p_{\rm sum})$. However, specifically in our situation, profile *1* in figure 25 corresponds to the graphs in figures 16 and 17. We see that the stiffness of the condensed phase (not too close to the critical point) is so high that even significant excesses of the binary pressure over the pressure $p_{\rm cr}$ only slightly shift the hydrodynamic profile relative to the binodal of pure gold on the plane ρ, T. Consequently, with moderate excesses of the pressure $p_{\rm sum}$ over the pressure $p_{\rm cr}$, corrections to the dependences for pure gold are small.

In the calculations given in sections 4–10, we used a 1D two-temperature hydrodynamic finite difference code partitioned by Lagrangian cells. In this code, water is adjacent to gold in the contact Lagrangian cell. In the contact cell, a chain of Lagrangian water cells borders a chain of Lagrangian gold cells. The used version of the code does not allow one to take into account the mutual diffusion of gold and water, since Lagrangian cells with the mixture are not provided. Accordingly, in our code there is no evaporation of gold into water with the formation of a diffusion mixture. Therefore, in all figures above, pure gold borders on pure water.

To justify our hydrodynamic modeling results, we note that the contribution of evaporation through the capillary barrier to the condensate production under our conditions is small. This contribution is small compared to the contribution to the condensate from gold with entropy above the critical value $s > s_{\rm cr}$, see figures 23–25. As a positive feature, we note that the code describes the formation of a layer of pure gold vapor at the interface between pure gold vapor and pure liquid gold. The beginning of the formation of such a vapor layer is seen in figures 18 and 19. A pronounced vapor layer *3*—*3*V is presented in figures 23 and 24.

We also note that the process of evaporation of gold into water was studied in detail in our previous works [48, 51, 54, 73, 76] using the molecular dynamics method.

11. Conclusions

The work described above is devoted to the analysis of laser shock waves. Such an analysis is important for laser shock peening (LSP) technology. A few years ago there was a branching of LSP methods. The technology with femtosecond (fs) LSP (fs LSP) [77] has been added to the traditional technology of nanosecond (ns) LSP [77]. Under femtosecond exposure (fs LSP), water flow around the target becomes unnecessary. But the special features of shock waves created by femtosecond generators are added. These features are almost unknown to experimentalists working with fs LSP.

These special features are associated with a short residence time of the material under shock loading. So called ultrashort shocks appear together with femtosecond loading. Sections 2 and 3 are devoted to theory of ultrashort shocks. Such a theory is necessary for understanding the phenomena associated with fs LSP technology.

In the case of ns LSP, the energy delivered by the laser through water to the target is limited by the optical breakdown of water. This condition imposes a very significant limitation on the amplitude of the shock wave. In case of fs LSP, energy is transmitted through air or even in a vacuum. Accordingly, the breakdown threshold is much higher. Femtosecond pulses are much brighter, because the pulse duration is many orders of magnitude shorter. Accordingly, the amplitudes of the shock waves in fs LSP technology are much higher. If in case of ns LSP the maximum amplitudes of the order of 1–10 GPa are reached, then in fs LSP technology megabar pressures are easily created. Of course, this is the advantage of femtosecond processing.

But there is a very serious drawback associated with fs LSP technology, which is as follows. The very essence of LSP (forging) is to create residual fields of plastic deformations and stresses. For this, the amplitude of the shock wave must exceed the threshold—Hugoniot elastic limit (HEL). Below this threshold, the shock wave propagates in the elastic mode and does not create plastic transformations. The drawback of fs action is that the HEL increases significantly (10–30 times) in the case of ultrashort shock waves (so called "superelasticity"). Therefore, creating permanent deformation is more difficult.

So, along with fs LSP technology, questions arise about the HEL threshold. Another problem analyzed in section 2 relates to elastic-plastic shocks–the problem important for LSP. It is known that with increasing pressure $p_{\rm pist}$ on a stationary piston supporting a shock wave, the wave structure changes. Below the HEL, a single uniform elastic shock wave (ElSW) runs in front of the piston. In the intermediate pressure range HEL $< p_{\rm pist} <$ OD a split elastic-plastic structure arises; OD means overdriven. This split structure consists of two jumps: ElSW jump running ahead and plastic shock wave (PlSW) behind the ElSW. Distance d between these jumps increases during their propagation. A single uniform PlSW propagates above the limit OD.

The refinement proposed in section 2 is as follows. Above the limit OD (which is ≈ 15 GPa for Al), a double structure arises. Namely, there is an ElSW in front of the PlSW. Moreover, the separation distance d, if averaged over time, remains constant—there is no jump spreading (increase of d with time) as in the split mode. Near the limit OD, the distance d can be large. This distance can significantly exceed those values d that were presented in the article [8]. In

this article, the existence of a two-wave structure moving as a whole was discovered. Laser shock waves created by fs or ns generators decay in the target volume. Attenuation determines the thickness of the forged area during LSP. These issues require additional analysis. The degree of attenuation is determined by the ratio of the thickness of the shock-compressed layer behind the shock wave to the radius R_{L} of the laser irradiation spot. Therefore fs shocks (ultrashort SW) decay much stronger with propagation distance. Attenuation increases when the shock wave travels a distance of the order of the radius of the spot.

High threshold HEL and fast attenuation both act in the direction of decreasing the thickness of the forged layer in fs LSP technology. Accordingly, in the case of fs LSP high initial pressures are required. Strong pressures are associated with strong heating. Strong heating causes melting and intense foaming of the surface layer [78]. Moreover, protective tapes are not used in fs technology (since the thickness of the forging is small); the tapes are used in ns LSP to prevent influence of heating.

Section 3 describes the melting and cavitation phenomena that accompany the heating by the fs pulse. Cavitation (appearance of cavities in liquid) is a strictly threshold phenomenon. If the cavitation threshold is significantly exceeded, foaming occurs. The greater the excess, the deeper the foaming process penetrates into the target volume. Section 3 presents the case near the cavitation threshold. Bubbles try to tear off the surface layer of the substance (spallation) but amount of absorbed energy is not enough to do this. Capillary force shrinks bubbles. At the same time, the cooling process proceeds. Bubbles are frozen in a solid matrix before they collapse completely. Section 3 describes thermomechanical stresses that form around frozen caverns.

Sections 4–10 describe the details of the ns LSP technology. As you know, to increase the mechanical efficiency in this technology (ns LSP) water is used. Therefore, the processes that occur with ns LSP (laser shock peening) and with ns LAL (laser ablation in liquid) are close. Although studied by different scientific communities.

In this work, the approach by Fabbro *et al* [49] is refined. The refinement consists in taking into account the pressure that continues to act both on the liquid and on the metal after the end of the laser pulse; according to the cited approach pressure should drops down to zero after the end of the pulse.

The expansion of the metal into the surrounding liquid during ns exposure is described in detail. This issue is important for ns LAL. The dynamic effect of melting on the formation of shock waves is described. It has been found that heating of a metal surface to supercritical entropy values plays an important role in the formation of a nanoparticle condensate—an important problem for ns LAL. A significant part of the condensate is formed from a metal whose entropy is higher than the value of entropy at a critical point. Nanoparticles of this part of the condensate do not appear as a result of evaporation from the surface of liquid metal. At ns LAL, the metal penetrates into the liquid mainly at the stage when the metal temperature is above the critical temperature. Under these conditions, metal and liquid are two freely miscible media. Mixing occurs due to intense mutual diffusion.

Acknowledgments

The work of INA and VVZ was supported by the Russian Science Foundation, grant No. 19-19-00697.

References

[1] Anisimov S I and Inogamov N A 1980 *J. Appl. Mech. Tech. Phys.* **21** 449
[2] Zhakhovsky V V, Migdal K P, Inogamov N A and Anisimov S I 2017 *AIP Conf. Proc.* **1793** 070003
[3] Zhakhovskii V V, Zybin S V, Nishihara K and Anisimov S I 1999 *Phys. Rev. Lett.* **83** 1175–8
[4] Anisimov S I and Medvedev Yu V 1988 *Sov. Phys. Tech. Phys.* **33** 1123–9
[5] Agranat M B *et al* 2010 *JETP Lett.* **91** 471–7

[6] Ashitkov S I, Agranat M B, Kanel' G I, Komarov P S and Fortov V E 2010 *JETP Lett.* **92** 516–20
[7] Zhakhovskii V V and Inogamov N A 2010 *JETP Lett.* **92** 521–6
[8] Zhakhovsky V V, Budzevich M M, Inogamov N A, Oleynik I I and White C T 2011 *Phys. Rev. Lett.* **107** 135502
[9] Inogamov N A, Zhakhovskii V V, Khokhlov V A and Shepelev V V 2011 *JETP Lett.* **93** 226–32
[10] Ashitkov S I, Komarov P S, Agranat M B, Kanel G I and Fortov V E 2013 *JETP Lett.* **98** 384–8
[11] Demaske B J, Zhakhovsky V V, Inogamov N A and Oleynik I I 2013 *Phys. Rev.* B **87** 054109
[12] Ashitkov S I, Komarov P S, Struleva E V, Agranat M B and Kanel G I 2015 *JETP Lett.* **101** 276–81
[13] Ashitkov S I, Komarov P S, Ovchinnikov A V, Struleva E V and Agranat M B 2016 *JETP Lett.* **103** 544–8
[14] Zhakhovsky V V, Demaske B J, Inogamov N A, Khokhlov V A, Ashitkov S I, Agranat M B and Oleynik I I 2012 *AIP Conf. Proc.* **1464** 102–12
[15] Zhakhovsky V V, Budzevich M M, Inogamov N A, White C T and Oleynik I I 2012 *AIP Conf. Proc.* **1426** 1227–32
[16] Demaske B J, Zhakhovsky V V, Inogamov N A and Oleynik I I 2010 *Phys. Rev.* B **82** 064113
[17] Albertazzi B *et al* 2017 *Sci. Adv.* **3** e160270
[18] Anisimov S I, Prokhorov A M and Fortov V E 1984 *Phys. Usp.* **27** 181–205
[19] Veiko V P, Volkov S A, Zakoldaev R A, Sergeev M M, Samokhvalov A A, Kostyuk G K and Milyaev K A 2017 *Quantum Electron.* **47** 842–8
[20] Saraeva I N, Kudryashov S I, Lednev V N, Makarov S V, Pershin S M, Rudenko A A, Zayarny D A and Ionin A A 2019 *Appl. Surf. Sci.* **476** 576–86
[21] Kudryashov S I, Samokhvalov A A, Nastulyavichus A A, Saraeva I N, Mikhailovskii V Y, Ionin A A and Veiko V P 2019 *Materials* **12** 562
[22] Kolobov Y R, Smolyakova M Yu, Kolobova A Yu, Ionin A A, Kudryashov S I, Makarov S V, Saltuganov P N, Zayarny D A and Ligachev A E 2014 *Laser Phys. Lett.* **11** 125602
[23] Ivanov D S, Blumenstein A, Ihlemann J, Simon P, Garcia M E and Rethfeld B 2017 *Appl. Phys. A* **123** 744
[24] Shih C Y *et al* 2018 *Nanoscale* **10** 6900–10
[25] Povarnitsyn M E and Itina T E 2014 *Appl. Phys. A* **117** 175–8
[26] Kabashin A V, Singh A, Swihart M T, Zavestovskaya I N and Prasad P N 2019 *ACS Nano* **13** 9841–67
[27] Kanel G I, Razorenov S V and Fortov V E 2004 *Shock-Wave Phenomena and the Properties of Condensed Matter* (Springer)
[28] Zaretsky E B and Kanel G I 2011 *J. Appl. Phys.* **110** 073502
[29] Wilkins M L 1999 *Computer Simulation of Dynamic Phenomena* (Springer-Verlag Berlin Heidelberg)
[30] Zaretsky E B and Kanel G I 2012 *J. Appl. Phys.* **112** 073504
[31] Kanel G I 2012 *AIP Conf. Proc.* **1426** 939
[32] Perriot R, Zhakhovsky V V, Inogamov N A and Oleynik I I 2014 *J. Phys.: Conf. Ser.* **500** 172008
[33] Zhakhovsky V V, Inogamov N A, Demaske B J, Oleynik I I and White C T 2014 *J. Phys.: Conf. Ser.* **500** 172007
[34] Sokolowski-Tinten K, Bialkowski J, Cavalleri A, von der Linde D, Oparin A, Meyer-ter-Vehn J and Anisimov S I 1998 *Phys. Rev. Lett.* **81** 224–7
[35] Inogamov N A, Petrov Yu V, Anisimov S I, Oparin A M, Shaposhnikov N V, von der Linde D and Meyer-ter-Vehn J 1999 *JETP Lett.* **69** 310–6
[36] Zhakhovskii V V, Inogamov N A and Nishihara K 2008 *JETP Lett.* **87** 423–7
[37] Ashitkov S I, Inogamov N A, Zhakhovskii V V, Emirov Yu N, Agranat M B, Oleinik I I, Anisimov S I and Fortov V E 2012 *JETP Lett.* **95** 176–81
[38] Inogamov N A *et al* 2015 *Eng. Failure Anal.* **47** 328–37
[39] Karthik D and Swaroop S 2017 *Mater. Manuf. Processes* **32** 1565
[40] https://en.wikipedia.org/wiki/lsp/technologies
[41] https://www.lsptechnologies.com/history.php
[42] Correa C, Peral D, Porro J A, Díaz M, Ruiz de Lara L, García-Beltrán A and Ocaía J L 2015 *Opt. Laser Technol.* **73** 179–87
[43] Lam J, Lombard J, Dujardin C, Ledoux G, Merabia S and Amans D 2016 *Appl. Phys. Lett.* **108** 074104
[44] Dyachkov S A, Parshikov A N, Egorova M S, Grigoryev S Yu, Zhakhovsky V V and Medin S A 2018 *J. Appl. Phys.* **124** 085902
[45] Sanz J, Linan A, Rodriguez M and Sanmartin J R 1981 *Phys. Fluids* **24** 2098–106
[46] Sanz J 1994 *Phys. Rev. Lett.* **73** 2700
[47] Inogamov N A, Zhakhovskii V V and Khokhlov V A 2015 *J. Exp. Theor. Phys.* **120** 15–48
[48] Inogamov N A, Zhakhovskii V V and Khokhlov V A 2018 *J. Exp. Theor. Phys.* **127** 79–106
[49] Fabbro R, Fournier J, Ballard P, Devaux D and Virmont J 1990 *J. Appl. Phys.* **68** 775–84
[50] Inogamov N A, Khokhlov V V and Zhakhovsky V A 2018 *JETP Lett.* **108** 439–45

[51] Khokhlov V A, Inogamov N A, Zhakhovsky V V and Petrov Yu V 2018 Formation of solitary microstructure and ablation into transparent dielectric by a subnanosecond laser pulse arXiv:1811.11990
[52] Petrov Yu V, Khokhlov V A, Zhakhovsky V V and Inogamov N A 2018 Laser-induced ablation of metal in liquid arXiv:1812.09109
[53] Khokhlov V A, Petrov Yu V, Inogamov N A, Migdal K P, Winter J, Aichele C, Rapp S and Huber H P 2019 *J. Phys.: Conf. Ser.* **1147** 012066
[54] Petrov Yu V, Inogamov N A, Zhakhovsky V V and Khokhlov V A 2019 *Contrib. Plasma Phys.* **59** e201800180
[55] Bushman A V, Kanel' G I, Ni A L and Fortov V E 1993 *Intense Dynamic Loading of Condensed Matter* (Taylor & Francis)
[56] Lomonosov I V and Fortova S V 2017 *High Temp.* **55** 585–610
[57] Khishchenko K V 2017 *Math. Montis.* **40** 140–7
[58] Khishchenko K V 2015 *J. Phys.: Conf. Ser.* **653** 012081
[59] Khishchenko K V 2008 *J. Phys.: Conf. Ser.* **121** 022025
[60] Khishchenko K V 1997 *High Temp.* **35** 991–4
[61] Inogamov N A, Zhakhovskii V V, Ashitkov S I, Khokhlov V A, Petrov Yu V, Komarov P S, Agranat M B, Anisimov S I and Nishihara K 2009 *Appl. Surf. Sci.* **255** 9712–6
[62] Inogamov N A, Ashitkov S I, Zhakhovsky V V, Shepelev V V, Khokhlov V A, Komarov P S, Agranat M B, Anisimov S I and Fortov V E 2010 *Appl. Phys. A* **101** 1–5
[63] Inogamov N A *et al* 2011 *Contrib. Plasma Phys.* **51** 367–74
[64] Ilnitsky D K, Khokhlov V A, Inogamov N A, Zhakhovsky V V, Petrov Yu V, Khishchenko K V, Migdal K P and Anisimov S I 2014 *J. Phys.: Conf. Ser.* **500** 032021
[65] Ashitkov S I, Zhakhovsky V V, Inogamov N A, Komarov P S, Agranat M B and Kanel G I 2017 *AIP Conf. Proc.* **1793** 100035
[66] Kanel G I, Zaretsky E B, Razorenov S V, Ashitkov S I and Fortov V E 2017 *Phys. Usp.* **60** 490–508
[67] Kanel' G I, Garkushin G V, Savinykh A S and Razorenov S V 2018 *J. Exp. Theor. Phys.* **127** 337–41
[68] Whitley V H, McGrane S D, Eakins D E, Bolme C A, Moore D S and Bingert J F 2011 *J. Appl. Phys.* **109** 013505
[69] Crowhurst J C, Armstrong M R, Knight K B, Zaug J M and Behymer E M 2011 *Phys. Rev. Lett.* **107** 144302
[70] Nigmatulin R I and Bolotnova R K 2011 *High Temp.* **49** 303–6
[71] Khokhlov V A, Inogamov N A, Zhakhovsky V V, Anisimov S I and Petrov Yu V 2014 *Proceedings of the Kabardino-Balkarian State University* **4** 53–9
[72] Inogamov N A, Zhakhovsky V V, Khokhlov V A, Demaske B J, Khishchenko K V and Oleynik I I 2014 *J. Phys.: Conf. Ser.* **500** 192023
[73] Inogamov N A, Khokhlov V A, Petrov Yu V and Zhakhovsky V V 2020 *Opt. Quantum Electron.* **52** 63
[74] Zhukhovitskii D I and Zhakhovsky V V 2020 *J. Chem. Phys.* **152** 224705
[75] Zhakhovsky V V, Kryukov A P, Levashov V Yu, Shishkova I N and Anisimov S I 2019 *PNAS* **116** 18209–17
[76] Petrov Yu V, Khokhlov V A, Zhakhovsky V V and Inogamov N A 2019 *Appl. Surf. Sci.* **492** 285–97
[77] Sano T, Eimura T, Kashiwabara R, Matsuda T, Isshiki Y, Hirose A, Tsutsumi S, Arakawa K, Hashimoto T, Masaki K and Sano Y 2017 *J. Laser Appl.* **29** 012005
[78] Fang R, Vorobyev A and Guo C 2017 *Light: Sci. Appl.* **6** e16256